



MINTEK

**Specialists in mineral and
metallurgical technology**

COMMUNICATION

C3644M/ GEN 810

**DEVELOPMENT OF A SMART ROCKBOLT FOR UNDERGROUND
MONITORING OPERATIONS**

FINAL REPORT

by

JS MOEMA, R PATON, & PV SCHEERS

CONFIDENTIAL

28 July, 2003

Chief Investigator: R Paton

Investigators: JS Moema, R Paton, & PV Scheers

Head – Ferrous Metals: R Paton

Manager – PMD: M Motuku

Technical Objective No.: 321

Project No.: 73089901/GEN 810

Client: SIMRAC

APPROVED
MANAGER

DATE

CHECKED
GROUP HEAD

DATE

CHECKED
AUTHOR

DATE

This document is issued as a means of rapid communication of information for the purpose of disclosure or discussion. Its distribution is restricted to persons appearing on the distribution list at the end. It may not be passed on to any other person; it may not be quoted as a reference or included in any bibliography. The contents may not be reproduced in part or in whole without permission from Mintek.

C3644M/GEN 810

DEVELOPMENT OF A SMART ROCKBOLT FOR UNDERGROUND MONITORING
OPERATIONS

FINAL REPORT

by

JS Moema, R Paton, & PV Scheers

28 July, 2003

PHYSICAL METALLURGY DIVISION

DEVELOPMENT OF A SMART ROCKBOLT FOR UNDERGROUND MONITORING
OPERATIONS

FINAL REPORT

by

JS Moema, R Paton, & PV Scheers

28 July, 2003

Chief Investigator: R Paton

Investigators: JS Moema, R Paton, PV Scheers, S Roberts
& CJ Fletcher

Head – Ferrous Metals: R Paton

Manager – PMD: M Motuku

Technical Objective No.: 321

Project No.: 73089901/GEN 810

Client: SIMRAC

SUMMARY

Rockbolting is a prerequisite for providing roof support in mining operations. The problem of rock pressure becomes worse as mining becomes deeper. Most of the rockbolts designs are made from simple carbon steel. The related problems of uncertainty as to the quality of installation of grouted steel tendons for reinforcement of rock around tunnels and stope gullies, and the effect of corrosion, rock deformation and repeated dynamic loading from seismic events on the integrity of even well installed tendons, have been long recognised both in South Africa and world-wide.

Support, which is adequate on installation, may be insufficient when loading conditions change. A smart rockbolt was therefore proposed that, when stressed underground, undergoes a microstructural transformation, with its properties changing from a non magnetic to magnetic depending on the degree of plastic deformation, thus leading to a change in longitudinal ultrasonic velocity. These properties can be monitored using a portable magnetic and ultrasonic instrument respectively to determine a change in loading conditions, and to warn of a possible overload condition. The smartbolt acts as a sensor for determination of stresses in mine workings. Also, since the smartbolt alloy could be installed in a mine containing aggressive minewater, the opportunity has been taken to study some of its corrosion properties.

This report detail the research work performed at Mintek for SIMRAC into the development of a sensor material (smartbolt alloy) using metastable austenitic stainless steel. This study was split in to two phases. Phase 1 investigated the use of magnetic methods in measuring the stress or microstructural transformation in an individual bolt in both laboratory and underground environment. The corrosion performance of the smartbolt alloy was evaluated in synthetic minewater and compared with that of AISI 304 and 316 as well as mild steel. Phase 2 investigated the use of ultrasonic methods, modelling of the smartbolt alloy and testing underground.

Phase 1: Mintek identified an alloy composition as being suitable for acting as a smartbolt material under the influence of strain. Laboratory work has shown that there is good correlation between ferritescope (magnetic) readings and those from a magnetic balance. Some problems do, however, exist with the ferritescope method of monitoring, in particular the depth of penetration. However, tests were carried out underground.

As a means of comparison, telltales (simple wire extensometers which give a visual warning of rock movement) were installed adjacent to some of the smartbolts. The results show a similar pattern developing at the two test sites chosen in that a gradual yielding of the bolts was taking place. Clearly, smartbolt technology was in its early stages, and more testing was required.

Phase 2: Characterisation have been performed under laboratory conditions and show that the smartbolt alloy has a good combination of high strength and ductility; this is important in order to resist extreme conditions of high tensile and shear stress, much as a conventional roof bolt. Comparisons have been made with standard grades such as Type 304 stainless steel including the work-hardening behaviour. Some preliminary modelling work has been carried out to assess the plastic behaviour of metastable austenitic stainless steels of which the smartbolt alloy is part.

A portable ultrasonic (USM 25 DAC) monitoring device was used to measure the longitudinal velocity during the calibration trials. The results show a good correlation between the longitudinal ultrasonic velocity and strain. Smartbolts of dimension 1.5m by 16mm and 1.5 m by 20 mm have been manufactured and installed by grouting and mechanical point anchored methods in platinum mine for monitoring. Using an ultrasonic sound velocity-measuring device, it is shown that a clear indication of stress in an individual bolt can be quickly and simply measured. A trend over a three months period is developing with each bolt yielding.

TABLE OF CONTENTS

	<i>Page</i>
1. INTRODUCTION.....	1
2. EXPERIMENTAL TECHNIQUE	2
2.1 <i>Industrial</i>	2
2.2 <i>Laboratory</i>	3
2.3 <i>Field testing</i>	5
3. RESULTS AND DISCUSSION.....	5
3.1 <i>Microstructure</i>	5
3.2 <i>Hardness</i>	8
3.3 <i>Tensile Properties</i>	9
3.3.1 Proof stress and UTS.....	9
3.3.2 Elongation to fracture.....	10
3.3.3 Strain hardening exponent.....	12
3.4 <i>Modelling load-strain characteristics of smartbolt alloy</i>	17
3.5 <i>Corrosion Properties</i>	21
3.6 <i>Bolt Calibration</i>	24
3.7 <i>Field testing</i>	27
4. CONCLUSIONS.....	31
5. REFERENCES.....	32
APPENDIX 1- BACKGROUND INFORMATION ON ULTRASONICS	34
APPENDIX 2- PRODUCTION ROUTE OF SMARTBOLT ALLOY	36
APPENDIX 3- OPERATION OF ULTRASONIC INSTRUMENT	37
APPENDIX 4- CORROSION PROPERTIES OF SMARTBOLT ALLOY	45

LIST OF TABLES

Table 1.	Chemical composition of the smartbolt alloy	3
Table 2.	Vickers test results (average of five measurements).....	9
Table 3.	Tensile tests results (12.5mm diameter specimen).....	10
Table 4.	Tensile tests results (6.25mm diameter specimen).....	10
Table 5.	Mechanical values of the analysed materials.....	11
Table 6.	Flow curve parameters for smartbolt alloy and Type 304 stainless steel.....	19
Table 7.	Corrosion rate values.....	20
Table 8.	Breakdown potential values.....	23
Table 9.	Ultrasonic velocity measurements of the stressed minibolts.....	25
Table 10.	Acoustic properties of several metals.....	25
Table 11.	Ultrasonic velocity measurements of the bent minibolts.....	27
Table 12.	Summary of the ultrasonic velocity results of smartbolts installed at platinum mine test site.....	30
Table 13.	Potential smartbolt warning guidelines.....	30

LIST OF ILLUSTRATIONS

Figure 1.	Rotary forging of smartbolt ingot and wire rods.....	3
Figure 2.	Microstructure of lab annealed Type 304 stainless steel.....	6
Figure 3.	Microstructure of hot rolled smartbolt alloy.....	6
Figure 4.	Microstructure of lab annealed smartbolt alloy.....	6
Figure 5.	Microstructure of industrial annealed smartbolt alloy.....	7
Figure 6.	Smartbolt alloy plotted on Schaeffler-De Long diagram.....	8
Figure 7.	Comparison of different steel grades in terms of strength and ductility combination.....	12
Figure 8.	Stress-strain curves of the smartbolt alloy and Type 304 stainless steel.....	14

Figure 9.	Variation of strain hardening exponent, n^* , for smartbolt alloy.....	15
Figure 10.	Variation of strain hardening exponent, n^* , for Type 304 stainless steel.....	15
Figure 11.	Percentage martensite versus percentage elongation for both smartbolt alloy and Type 304 stainless steel.....	16
Figure 12.	Tensile and work-hardening rate curves for smartbolt alloy.....	16
Figure 13.	Tensile and work-hardening rate curves for Type 304	17
Figure 14.	Verification of the transformation-deformation function for smartbolt alloy.....	20
Figure 15.	True stress and predicted stress as a function of strain for smartbolt alloy.....	20
Figure 16.	Corrosion rates as a function of pH.....	22
Figure 17.	Corrosion rates as a function of time.....	22
Figure 18.	Corrosion rates as a function of the raw materials cost.....	23
Figure 19.	Chloride ion concentration (ppm).....	24
Figure 20.	Ultrasonic sound velocity versus strain for smartbolt alloy.....	26
Figure 21.	Schematic of 450mm minibolt before and after bending.....	27
Figure 22.	The drilling stage prior to installation of the required roofbolt at a platinum mine.....	28
Figure 23.	Monitoring of a smartbolt with a flat base plate using an ultrasonic measuring device.....	29
Figure 24.	Graphical presentation of the results obtained from a platinum mine test site.....	31

1. INTRODUCTION

This report detail the research work performed at Mintek for SIMRAC into the development of a smart rockbolt for underground monitoring using metastable austenitic stainless steel. This study was split into two phases as follows:

Phase 1

The objective of the first phase of this project was to investigate the use of magnetic methods in measuring the stress or microstructural transformation in an individual bolt in both laboratory and underground environment. In this phase (C3119M)⁽¹⁾, the smartbolt alloy's magnetic response to temperature change was particularly investigated. Laboratory characterisation (tensile tests at temperature range from 23° to 200°C) and magnetic (ferritescope, magnetic balance, X-ray diffraction) tests were carried out on mini and maxi (full-size) bolts. The influence of probe test position and the surface condition of the material (heat treatment scale) were also studied.

Using in-house laboratory built pulse-echo equipment, some preliminary data using the ultrasonic method were obtained and looked promising. For field testing, full-size bolts (~1.5m long) were prepared and installed in two sites, viz., a coal and gold mine respectively. Monitoring of the loading of the bolts was carried out monthly using a magnetic method. Some problems do, however, exist with ferritescope method of monitoring, in particular the depth of penetration. It was therefore recommended that ultrasonic technique be used or explored for monitoring as they may have certain advantages versus magnetic methods.

Phase 2

The results and recommendations of phase 1 led to the initiation of phase 2. It forms part of the work to explore ultrasonic velocity measurement technique for the nondestructive estimation of ferrite content in this metastable smartbolt alloy. In order to provide a more complete description of the alloy's behaviour, its response to stress and strain has been investigated. It also includes a full laboratory characterisation and preliminary modelling of a smartbolt alloy.

A suitable portable ultrasonic instrument was purchased and used to carry out the calibration and monitoring of the smartbolts. Since ultrasound techniques are described in the report, a brief summary of longitudinal velocity and its evaluation is given in **Appendix 1** to enable the reader to follow the discussion. Also, since the smartbolt alloy could be installed in a mine containing aggressive minewater, the opportunity has been taken to study some of its corrosion properties (**section 3.5 and Appendix 4**)

2. EXPERIMENTAL TECHNIQUE

2.1 Industrial

Two octagonal one ton ingots of smartbolt material were successfully rotary forged down to a section size of 140 mm square. The forged billets were soaked at 1200 °C, put through the roughing mill and finally through the 12-stand bar mill (Figures 1a and 1b). Rolling to wire rod (20 mm in diameter) was successfully carried out and an approximate 100 % yield was obtained. The rod material was annealed and water quenched (heat-treated) and then taken for rockbolt manufacture and calibration of individual bolts. A detailed processing route is shown in **Appendix 2**.

Important aspects in developing smart strain-sensitive materials are that the incubation strain is reduced as much as possible and that the microstructural transformation rate is high, thus enabling effective monitoring. Also they should not be too sensitive to process variability. The M_d temperature (the upper temperature at which transformation to martensite may be induced by deformation) of this alloy was determined in Phase 1 of the project and found to be somewhere around 120°C to 160°C (a value of 140°C with a precision of $\pm 20^\circ\text{C}$). The M_d temperature is dependent on the chemistry of the alloy, therefore the nominal specification of the smartbolt alloy was chosen (Table 1) from the range of composition studies. The smartbolt alloy was analysed using spark emission spectroscopy.

The chemical composition of this alloy is given in Table 1. A Ferriscope (Fischer MP3 model) and a permanent magnet was used to check that the material was non-magnetic before any laboratory work was carried out.



a.



b.

Figure 1. (a) Rotary forging of smartbolt ingot. (b) batches of smartbolt wire rod (20 mm in diameter).

Table 1. Nominal and analysed composition of the smartbolt alloy (wt%)

	Elements (wt%)										
	C	Si	Mn	P	S	Cr	N	Mo	Cu	Al	Sn
Nominal	0.2* min	-	8 to 12 ⁺	0.025 max	0.025 max	11 to 13 [#]	0.1 max	-	-	-	-
Analysed (spectroscopy)	0.233	0.61	9.99	0.014	0.0091	12.5	0.13	0.02	0.07	0.004	0.002

* preferably 0.25 ± 0.02 , + preferably 10 ± 1.0 , # preferably 11.5 to 12.5

2.2 Laboratory

Metallography was carried out by way of automated grinding and polishing. Hot rolled, laboratory and industrial annealed specimens were mechanically polished to a $1\mu\text{m}$ finish using diamond paste, and finally electropolished in 20 percent perchloric acid at 18 volts for 30 seconds (20ml perchloric acid plus 80ml alcohol) followed by etching in Beraha's reagent. Electrochemical polishing was necessary to remove any deformation-induced martensite that may have formed during the mechanical polishing.

For the determination of mechanical properties on hot rolled (HR), industrial (HRA) and laboratory annealed (HRL) material, standard (ASTM E8) round tensile specimens of 12.5 mm diameter and 50 mm gauge length of smartbolt alloy and Type 304 stainless steel were machined. Duplicate tensile tests using a Tinius Olsen 600kN tensile testing machine were carried out. The specimens were tested to the requirements of ASTM E8⁽²⁾. The samples were tested to failure at room temperature. For each test, the yield strength (at 0.2 per cent offset), tensile strength and per cent elongation were recorded.

Also, for the determination of work-hardening coefficient (n-value), tensile tests were carried out on laboratory annealed smartbolt alloy and Type 304. These samples were round tensile specimens of 6.25 mm diameter and 25 mm gauge length. Prior to testing, all the test specimens were wrapped with stainless steel foil and annealed at 1050°C followed by water quenching. The specimens were also tested to the requirements of ASTM E8⁽²⁾. Duplicate tensile tests using a computer interfaced Instron 1175 tensile machine (which allowed the data to be captured on a computer file), were carried out at a constant crosshead speed of 2 mm/min (initial strain rate of $1.3 \times 10^{-4} \text{s}^{-1}$). This strain rate was considered to be sufficiently low to prevent excessive local heating (adiabatic) in the specimen. The samples were tested to failure at room temperature.

Some preliminary modelling work was carried out to assess the plastic behaviour of these metastable austenitic stainless steels of which the smartbolt alloy is part. Microsoft's Excel SOLVER package was used as the computational tool to analyse the load-strain data.

To study the influence of stress and strain on industrial annealed smartbolt material and correlate the results with ultrasonic sound velocity, a series of mini bolts (approximately 750 mm in length) were tested using a Tinius Olsen 600kN frame. A Krautkramer USM 25 ultrasonic measuring instrument was used to measure the sound velocity of the mini-bolts at different strain levels. Calibration of the instrument was performed according to ASTM E494-75⁽³⁾ and the Krautkramer operating manual⁽⁴⁾. A detailed calibration process is shown in **Appendix 3**. It should be noted that Case A calibration process was used and Type 304 taken as a reference material.

2.3 Field testing

It was found that the proposed test site used 16mm and 20mm diameter roofbolts, therefore, some of the 20mm stock material was machined down to 16mm in diameter and these test bolts were re-heat treated. The threads (M16 RH and M20 RH) of the bolts were machined according to SABS 1408 of 1987 (code 142007 and 142037). The thread was approximately 150mm in length.

The smartbolts were not thread rolled because the material displays a much stronger work-hardening effect. In order to thread roll the material a special set of dies with high hardness is required. Two sets of smartbolts (six of 1.5m x 20mm and five of 1.5m x 16mm) were installed in a gully section at a platinum mine.

The first set of smartbolts was resin bonded and the other set was mechanically anchored in order to compare the two different methods of installation (It is felt that the technology is more appropriate using anchoring rather than frictional forces). Monitoring of the loading on the bolts was carried out monthly.

3. RESULTS AND DISCUSSION

3.1 Microstructure

The microstructure of Type 304 in the laboratory-annealed condition is shown in Figure 2. Figures 3 to 5 show the microstructure of the smartbolt alloy in different process conditions. The hot rolled specimen shows some undissolved carbide at the grain boundaries (Figure 3). The laboratory and industrial annealed microstructures were similar (fully austenitic) with no presence of carbides (Figures 4 and 5).

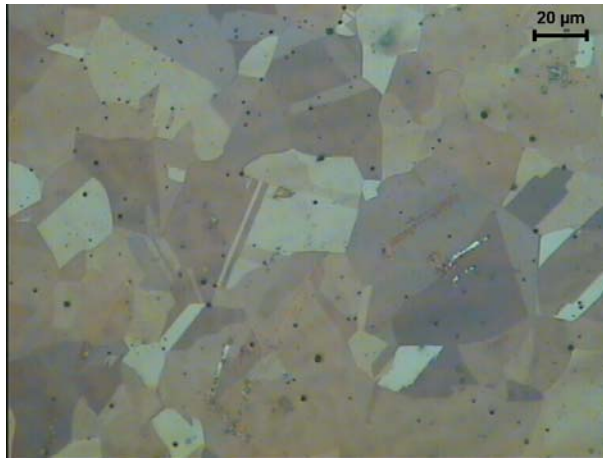


Figure 2: Microstructure of laboratory annealed Type 304 that shows an austenitic structure

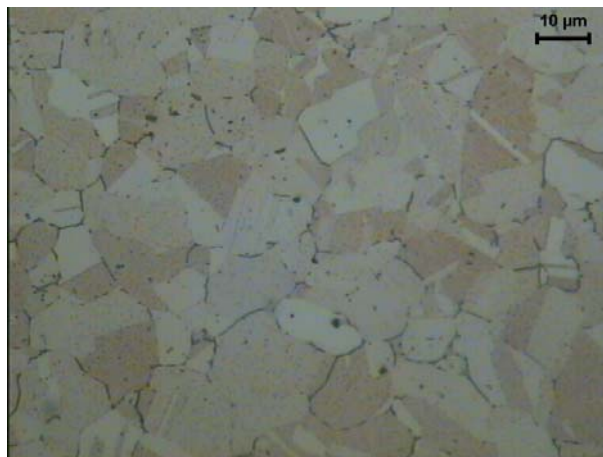


Figure 3: Microstructure of hot rolled smartbolt alloy that shows some undissolved carbides

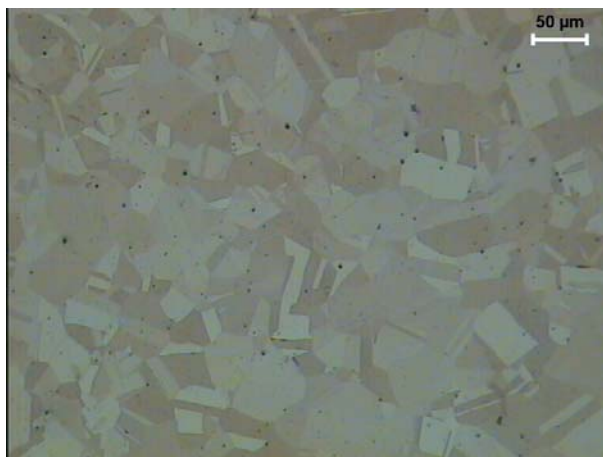


Figure 4: Microstructure of laboratory annealed smartbolt alloy that is fully austenitic and free of carbides

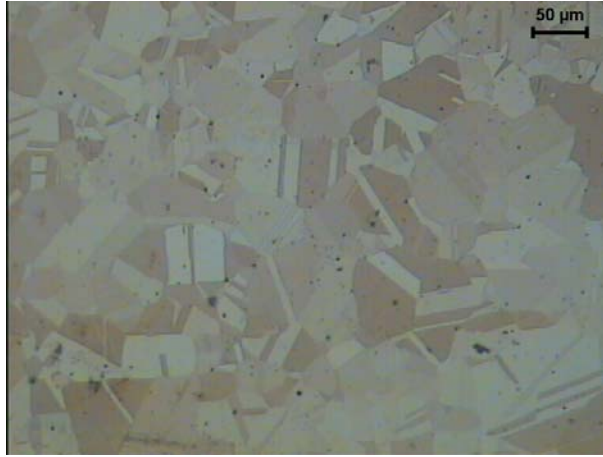


Figure 5: Microstructure of industrial annealed smartbolt alloy that is fully austenitic and free of carbides

The black spots seen in these micrographs are non-metallic oxide inclusions. Martensite was not detected in the alloy in the hot rolled and annealed state because the Ms temperature (temperature at which martensite start to form) was calculated to be below room temperature ($M_s (^{\circ}C) = 502 - 810C - 1230N - 13Mn - 30Ni - 12Cr - 54Cu - 46Mo$). Schaeffler/De Long and Hull coefficients were used to predict the phase composition of the alloy. The predicted composition is shown to be in the austenite plus martensite region (Figure 6). The predicted phase composition was plotted on the Schaeffler⁽⁵⁾ diagram using the following empirical formulae with standard coefficients for each element:

$$Ni_{eq} = Ni + 0.5Mn + 0.3Cu + 30C + 20N \dots (\text{Schaeffler/De Long}) \quad (1)$$

$$Ni_{eq} = Ni + 0.11Mn - 0.0086Mn^2 + 30C \dots (\text{Hull}) \quad (2)$$

$$Cr_{eq} = Cr + Mo + 1.5Si$$

Manganese is one of the austenite formers, therefore a significant change in its coefficient has influenced the nickel equivalent of the alloy as shown on the graph (point 1 and 2 by Schaeffler/De Long and Hull coefficients).

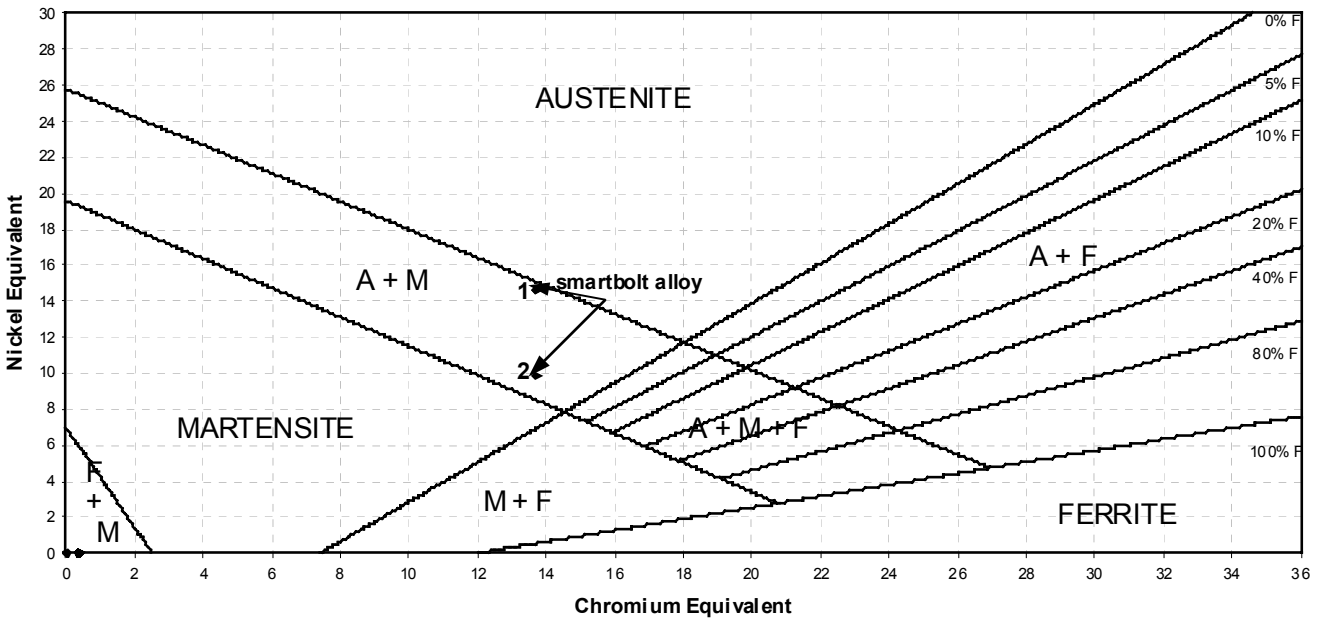


Figure 6. Smartbolt alloy plotted on Schaeffler-De Long diagram using Schaeffler and Hull equivalents

3.2 Hardness

Vickers hardness tests using a 20kg load were performed on hot rolled and annealed specimen (two from each batch), taken at random from the supplied bars. The results of these tests including the standard deviation are summarised in Table 2. The hardness value of the smartbolt alloy in the hot rolled state is somewhat higher than that in the annealed state; this is probably due to complete recrystallization taking place during annealing, producing softening. It can be seen that the smartbolt alloy is substantially harder than Type 304 stainless steel partly due to its much higher carbon and nitrogen contents.

Table 2. Vickers hardness test results (average of five measurements)

		Hardness (HV₂₀)	
Sample	Condition	Average	Standard deviation
Type 304	Lab annealed	177.5	5.2
Smartbolt	Hot rolled	295.3	7.3
Smartbolt	Lab annealed	274.2	9.3
Smartbolt	Industrial annealed	261.2	9.6

3.3 Tensile Properties

The mechanical properties of the alloys are described in the following sections. The tensile properties for the alloys tested at room temperature are summarised in Tables 3 and 4.

3.3.1 Proof stress and UTS

The annealed proof values are fairly similar to the current carbon steel grade used for roofbolts. The standard deviation is also included. The proof stress of the smartbolt alloy in the HR and HRL condition is 524 and 451MPa respectively, which is somewhat higher than that for Type 304 (319MPa). The somewhat higher yield stress obtained from the hot rolled material might be due to undissolved carbides on grain boundaries, also incomplete recrystallisation after rolling. Therefore, it is preferable to use the material in the annealed condition. Typical values for the tensile strength of industrial Type 304 are 560 to 635MPa.

The UTS of the smartbolt alloy in the HR and HRL condition was 847MPa and 961 to 1039MPa for the laboratory and industrial annealed material, respectively. The UTS values, relative to the proof stress values, are an indication of the instability of the alloy. It is clear that the smartbolt alloy is the most unstable alloy, and has a relatively high ratio of UTS/Proof.

3.3.2 Elongation to fracture

The percentage elongation for Type 304 obtained in this work was 80%. This value is high due to the small gauge length chosen (the minimum elongation specified for Type 304 is 40%), compared to that of the smartbolt alloy, which is 25 to 30%. TRIP (Transformation Induced Plasticity) formation in Type 304 does lead to an increase in work hardening rate and an increase in resistance to necking. In the smartbolt material, alpha prime (α') martensite is nucleated very quickly and hence large amounts of α' martensite will reduce the % elongation (as shown in Figure 8) and produce a characteristic flat-face fracture.

Table 3. Tensile tests results (12.5mm diameter specimen)

Alloy	UTS (MPa)	0.2%Proof Strength (MPa)	Elongation (%)	Condition
Smartbolt	847 \pm 23	524 \pm 26	18	Hot rolled
Smartbolt	1039 \pm 41	445 \pm 21	29	Lab annealed
Smartbolt	961 \pm 9.0	451 \pm 39	25	Industrial annealed

Table 4. Tensile tests results (6.25mm diameter specimen)

Alloy	UTS (MPa)	0.2%Proof Strength (MPa)	Elongation (%)	Condition
Type 304	733 \pm 1.0	319 \pm 63	83	Lab annealed
Smartbolt	1063 \pm 24	438 \pm 2.0	30	Lab annealed

Doege and Kulp⁽⁶⁾ investigated the forming behaviour and properties of both L-TRIP (TRIP700) and H-TRIP (Type 304) steel types. TRIP-steels contain austenite, which is metastable at room temperature. It transforms to martensite during straining (TRIP effect). This process improves the strength to ductility balance of these steels, i.e. the product of strength and ductility.

These compare fairly well with smartbolt alloy, but the ductility of L and H TRIP steels is higher; however their strength is lower. The mechanical results of these TRIP-steels are compared with those of the smartbolt alloy, i.e. Table 5 with Tables 3 and 4.

Table 5. Mechanical values of the analysed materials⁽⁷⁾

Material	s_o mm	RD °	A_g %	A₈₀ %	YS MPa	UTS MPa
L TRIP	1.50	0	25	31	436	719
TRIP700		45	24	28	441	719
		90	23	27	453	726
H TRIP	1.00	0	44	48	316	625
AISI304		45	47	52	296	581
		90	48	53	293	582

Where: **RD** is the rolling direction, **A_g** is uniform elongation and **A₈₀** is the percentage elongation at fracture

For the last 20 years, the steel industry introduced new steel categories such as high strength low alloy steels (HSLA), the interstitial free high strength steels (IF-HS), and the dual phase steels (DP-steels)⁽⁷⁾. However, for the past 10 years the investigation of TRIP steels has been investigated and as can be seen from Figure 7, their mechanical properties are somewhat different from all the previous steel grades.

TRIP steels can offer a much better combination of strength and ductility. The product of high yield strength and uniform ductility of a smartbolt alloy is slightly higher than that of the TRIP steels. By extrapolating Figure 7, it can be seen that the smartbolt alloy lies to the right hand side of the TRIP grades, which have a strength and ductility product of about 20000MPa.

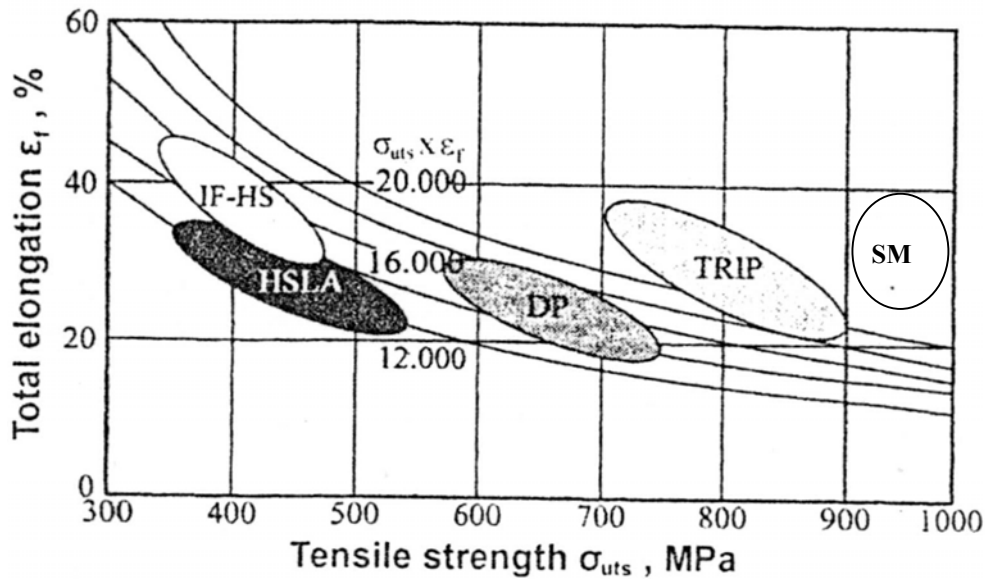


Figure 7. Comparison of different steel grades in terms of strength and ductility combination⁽⁷⁾

3.3.3 Strain hardening exponent (n)

The smartbolt alloy exhibits an inflection in the stress-strain curve as compared to Type 304. (see Figure 8). The deformation-induced martensitic transformation gives a striking effect on the tensile flow curve of this alloy. As more martensite is formed during continued straining, and because this martensite is strong, the flow stress rapidly increases as the martensite itself starts to participate in the deformation. The high work-hardening rate produced by the martensite being deformed, more than counterbalances the transformation-induced strain, i.e. the transformation plasticity.

The plots for strain hardening exponent, n^* (instantaneous n -value) versus strain (ϵ) for smartbolt and Type 304 are shown in Figures 9 and 10 respectively. Trendlines have been superimposed on the data, for convenience, using least-squares polynomial regression. It can be seen that there are two extreme forms of behaviour between the two alloys.

The rapid increase in the rate of strain hardening in the smartbolt alloy is the result of the strain-induced transformation of austenite to martensite in the specimen gauge length during testing. The maximum rate of this transformation is said by Fang⁽⁸⁾ to occur at the lowest rate of strain hardening. This corresponds to the noticeable dip in hardening observable at the start of the curve. The value of n^* for smartbolt alloy in these dips is between 0.10 and 0.15 which is higher than that of Type 304 (less than 0.10). The work-hardening rate initially decreases as deformation of the austenite occurs. The interaction of the dislocations and martensite during subsequent deformation is responsible for the rapid increase in the value of n^* at greater amounts of strain.

Smartbolt alloys exhibit a rapid increase in n^* value, which peaks at between 10 and 20% strain, then declines. The peak value reached by n^* in this alloy is of the order of 0.75. Type 304 exhibits a slowly increasing value of n^* , which scarcely changes for strains above 30%. The maximum value of n^* reached in this alloy is about 0.55.

Figure 11 show the amount of martensite (measured as percent magnetism) formed during testing as a function of percent elongation. It is clear that the smartbolt alloy undergoes transformation during the early stages of plastic behaviour unlike the commercial Type 304 which has a higher incubation period and requires at least 20% plastic strain to give a measurable response. It can be seen that the incubation strain of the smartbolt alloy is reduced and that the microstructural transformation rate is high, thus enabling effective monitoring.

In order to understand the maximum uniform elongation (true strain based only on the strain up to maximum load, ϵ_u), the work-hardening rate ($\delta\sigma/\delta\epsilon$) of the smartbolt alloy and Type 304 stainless steel was determined as a function of strain and superimposed on the tensile curve information (Figures 12 and 13). The maximum uniform elongation is governed by the shape of the ($\delta\sigma/\delta\epsilon$) versus (ϵ) curve. For the smartbolt alloy, the work-hardening rate yields a local minimum and a local maximum before it finally decreases with increasing strain (Figure 12).

It must be noted that necking occurs at a strain at which the slope of the true stress-true strain curve equals the true stress at that strain, i.e. $\delta\sigma/\delta\varepsilon = \sigma^{(9)}$. However, the smartbolt alloy does not show any evidence of necking. It fails prematurely due to the formation of martensite at a stress value above 2000MPa and shows a flat face fracture. This is because of a high transformation of austenite to martensite.

For Type 304 stainless steel, the work-hardening rate ($\delta\sigma/\delta\varepsilon$) continues to decrease as a function of strain (ε), and $(\delta\sigma/\delta\varepsilon) = \sigma$, occurs at a value of strain (approx. 0.51). Therefore, the two curves meet at a strain of approximately 0.51 and stress value below 2000MPa, Figure 13. Thus the ductility is enhanced in Type 304 as the rate of transformation is slower and necking adds to the total elongation.

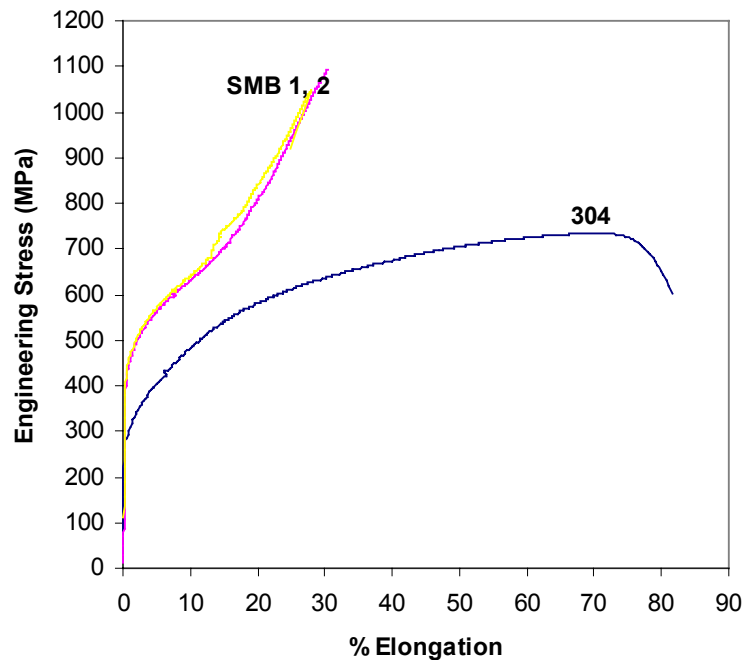


Figure 8. Comparison of stress-strain curves of the smartbolt alloy and Type 304 stainless steel

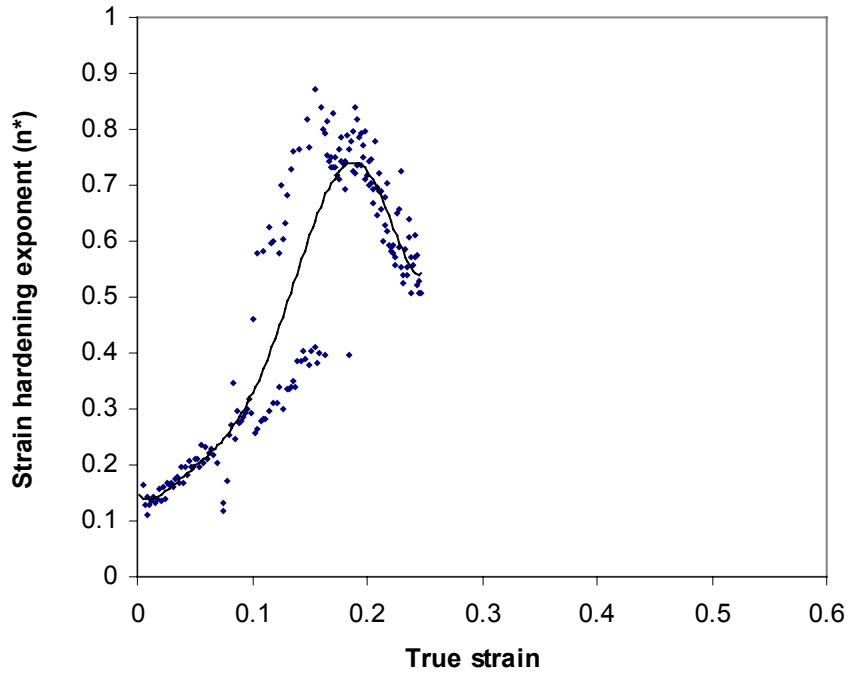


Figure 9. Variation of strain hardening exponent, n^* , for smartbolt alloy

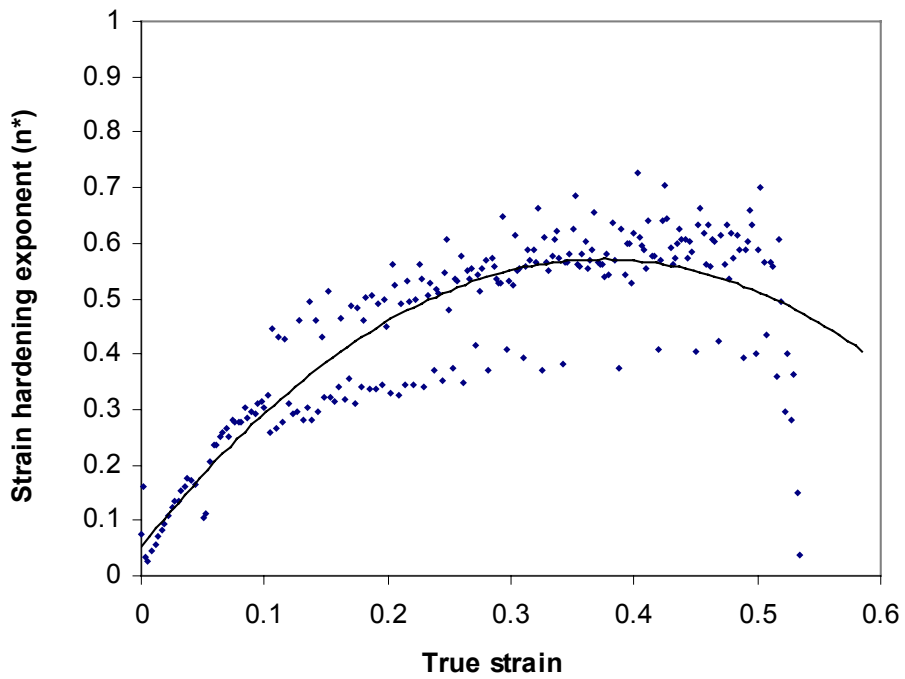


Figure 10. Variation of strain hardening exponent, n^* , for Type 304

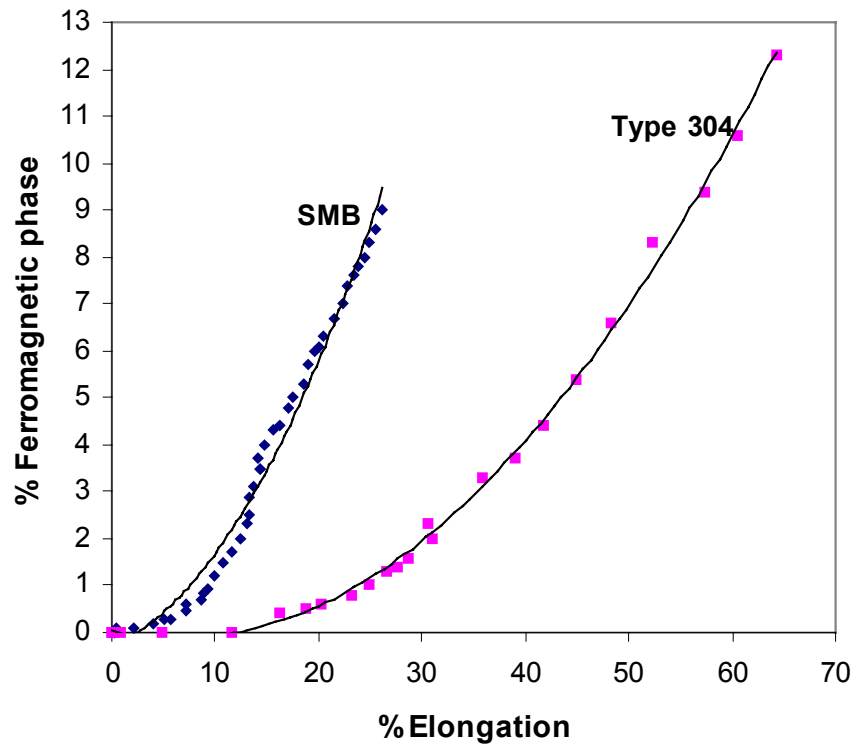


Figure 11. Percentage ferromagnetic phase versus percentage elongation for smartbolt alloy and Type 304 stainless steel as determined by a ferritescope

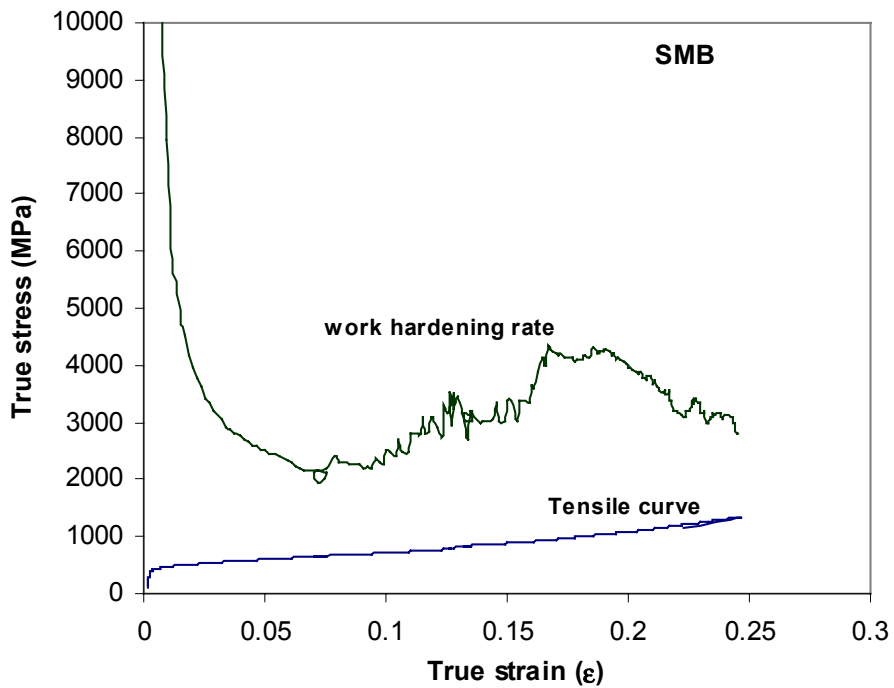


Figure 12. Tensile and work hardening rate curves for smartbolt alloy

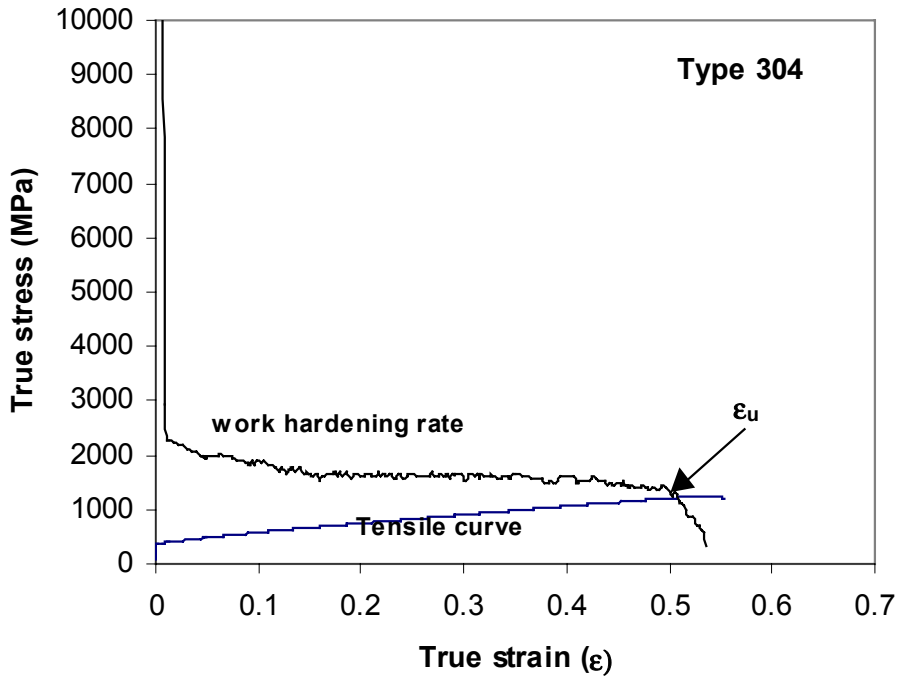


Figure 13. Tensile and work hardening rate curves for Type 304 stainless steel

3.4 Modelling load-strain characteristics of smartbolt alloy

This part of the work was undertaken to derive and verify a model for the plastic behaviour of the smart alloy together with a standard Type 304 stainless steel, both alloys being metastable with regard to the austenitic structure. The differences between a so-called ‘smart’ material and other materials can thus be quantified.

It has been found that the flow curve for many materials can be empirically described by the equation:

$$\sigma = K[\ln(1 + e)]^n \dots\dots\dots (1)$$

where σ = true stress, e = true strain, K = austenitic ‘strength factor’ (constant) and n = ‘strain-hardening index’ (constant).

Literature⁽¹⁰⁾ however, reports that for some engineering materials like ‘18-8’ stainless steel, the expression does not hold, and it is suggested that a strain-induced decomposition of austenite to martensite is responsible for this effect.

Ludwigson and Berger⁽¹⁰⁾ have therefore proposed an amended flow curve equation to incorporate both the true stress contribution of austenite at any level of strain and the true stress contribution of martensite at any level of strain:

$$\sigma = K[\ln(1 + e)]^n \left[1 - \left(1 + \frac{e^{-B}}{A} \right)^{-1} \right] + C \left(1 + \frac{e^{-B}}{A} \right)^{-Q} \dots\dots\dots (2)$$

Where A = a constant representing the propensity of the material to transform to martensite, B = a constant to account for autocatalysis, C = martensitic ‘strength factor’ (constant) and Q = martensitic ‘strengthening index’ (constant).

The writers also showed that the volume fraction of martensite (VFM) could be related to the volume fraction of austenite (VFA) in metastable austenitic stainless steels by equation:

$$VFM = Ae^B (VFA) \dots\dots\dots (3)$$

Since, the sum of VFM and VFA is unity, equation (3) can be rewritten as:

$$\frac{VFM}{(1 - VFM)} = Ae^B \dots\dots\dots (4)$$

and taking the logarithm of the expression above, thus yields:

$$\log \left[\frac{VFM}{(1 - VFM)} \right] = \log A + B \log e \dots\dots\dots (5)$$

A plot of $\log [VFM/(1-VFM)]$ versus $\log [e]$ therefore gives a straight line with slope equal to ‘ B ’ and y-intercept equal to ‘ $\log A$ ’. Using this relationship, the A and B values for the particular material can be determined (Figure 14). The remaining four constants, K , n , C and Q , can then be determined by obtaining a best-fit approximation of the available experimental data.

From experiment, a range of data relating measured true stress, $\sigma_{measured}$, and true strain, e , is obtained. Equation (2) relates the unknown constants to a calculated true strain, $\sigma_{calculated}$.

The constants can then be calculated by minimising the sum of the square of the difference (i.e. error) between $\sigma_{measured}$ and $\sigma_{calculated}$. Microsoft's Excel SOLVER package was used as the computational tool.

The software relies on an initial best guess of the unknown constants, and through a series of non-linear regressions, modifies the values for K , n , C and Q such that over the entire range of experimental data, $\Sigma(\sigma_{measured} - \sigma_{calculated})^2$ is as small as possible.

In order to verify the results obtained, a plot of $\sigma_{measured}$ versus $\sigma_{calculated}$ can be made, and if sufficiently accurate numerical values for the unknown constants have been calculated, the plot should yield a straight line with slope equal to unity and a y-intercept equal to zero (Figure 15). The constants measured for both steels are shown in Table 6 below.

Table 6. Flow-curve parameters for smartbolt alloy and Type 304 stainless steel

Alloy	K (MPa)	n	C (MPa)	Q	A	B
Type 304	1200	0.35	1735	0.73	0.49	2.72
Smartbolt	900	0.14	6690	1.04	1.98	2.16

The parameter C is the martensite analogue of the austenitic strength factor K . It can be seen that C is much higher in the smartbolt alloy, reflecting the higher carbon content relative to Type 304. Conversely, K is somewhat higher in Type 304 due to its higher alloy content. The lower n value for the smartbolt alloy reflects work hardening of martensite rather than austenite (see propensity to transform A value). The transformation response (A value) for the smartbolt alloy is about four times higher than Type 304 stainless steel.

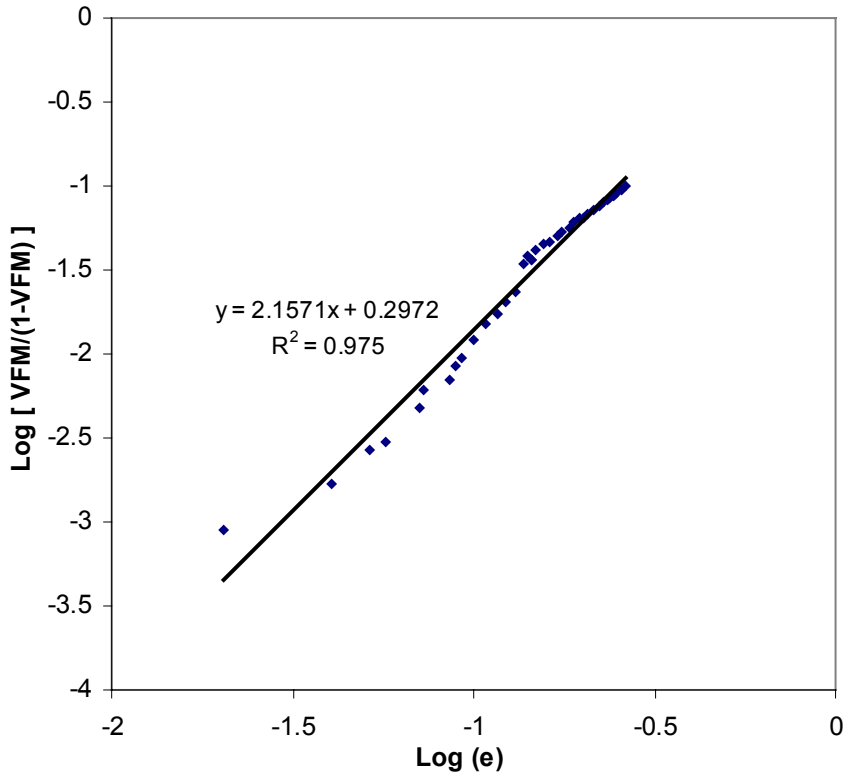


Figure 14. Verification of the transformation-deformation function for smartbolt alloy

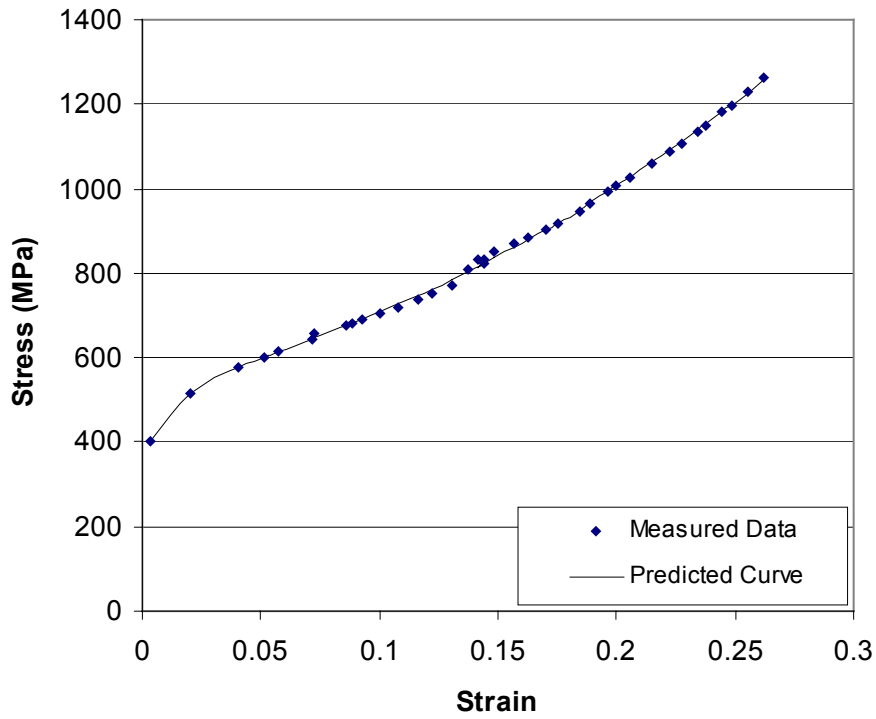


Figure 15. True stress and predicted stress as a function of strain for smartbolt alloy

3.5 Corrosion Properties

The corrosion performance of the 12Cr-9Mn-C steel (smartbolt alloy) was evaluated in synthetic mine water and compared with that of AISI 304 and 316 as well as mild steel. The corrosion rates of the various materials are given as a function of pH in Figure 16.

The corrosion rate of the 12Cr-9Mn-C steel (smartbolt alloy) is more than two orders of magnitude lower than that of mild steel and one order of magnitude higher than that of AISI 316. The value close to 0.01 mm/y over a large pH range is quite acceptable, but the corrosion rate increases sharply below pH 4. However, measurements of the corrosion rate of the 12Cr-9Mn-C steel and AISI 316 as a function of time at pH 3 (Figure 17) indicate that in the case of the 12Cr-9Mn-C steel, the corrosion rate drops significantly in the first 10 hours and reaches the value observed at higher pHs. The potential increases from -0.050 V to -0.025 V, and it appears thus that some passivation is taking place.

Figure 18 compares the corrosion rates as a function of the raw materials cost (October 1998). It can be seen from Figure 18 that an initial threefold increase in cost (12Cr-9Mn-C compared to mild steel) lowers the corrosion rate by more than two orders of magnitude, but that a further threefold increase in cost only reduces the corrosion rate by a factor of three. This places the 12Cr-9Mn-C steel in a very favourable position.

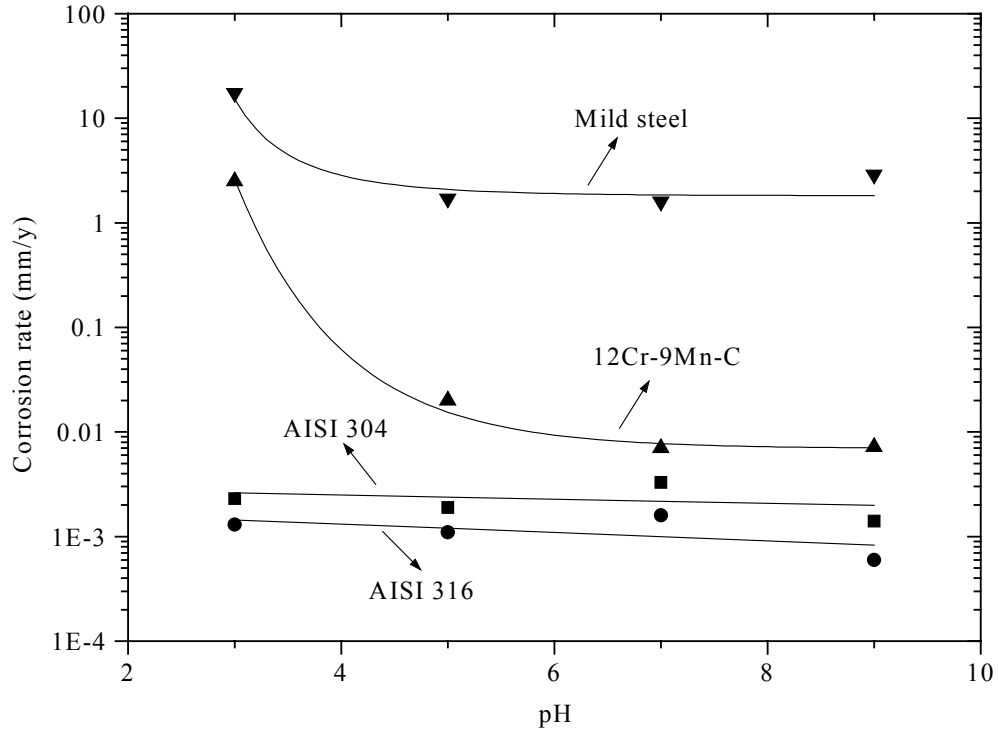


Figure 16. Corrosion rates as a function of pH

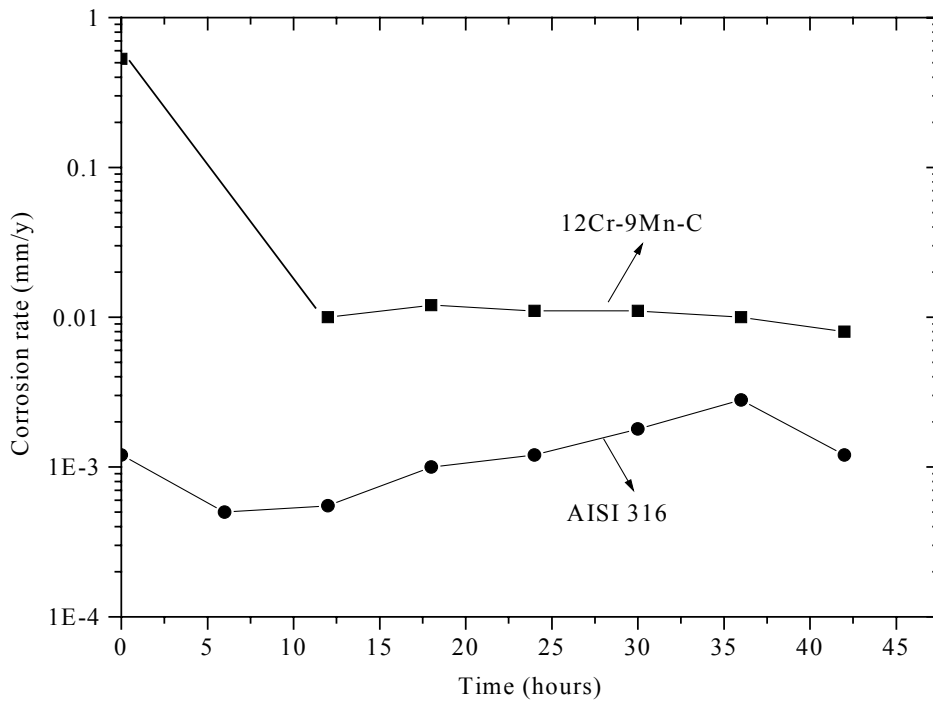


Figure 17. Corrosion rates as a function of time (pH 3)

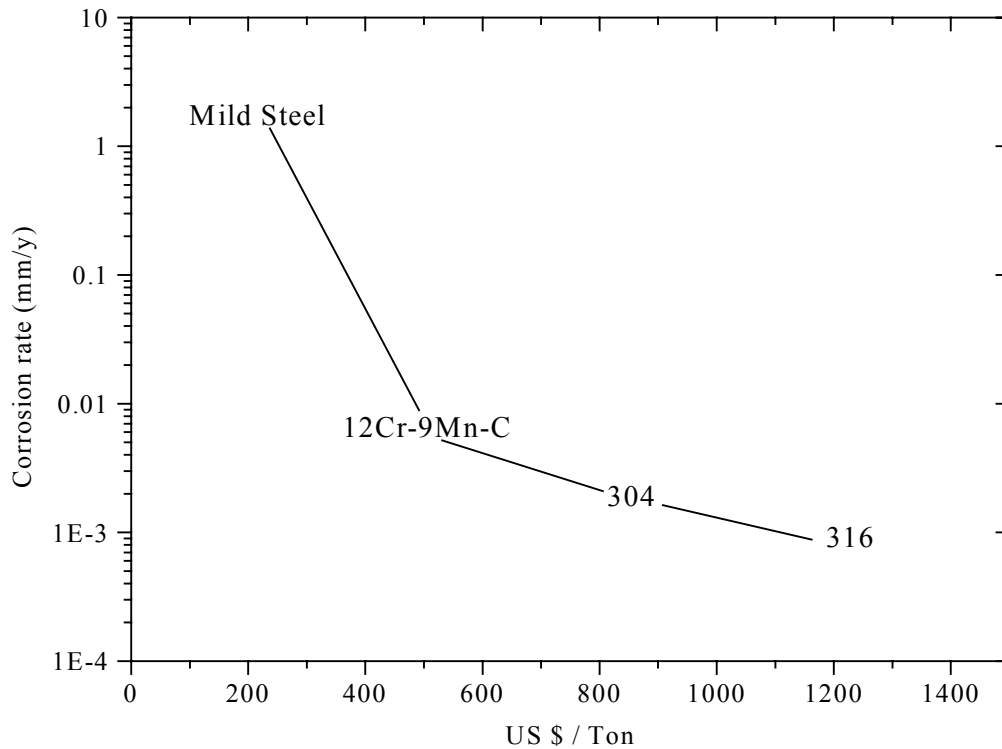


Figure 18. Corrosion rates as a function of the raw materials cost

The breakdown potential values of the 12Cr-9Mn-C steel and AISI 316, determined from cyclic polarisation scans in mine water with various chloride concentrations, are represented graphically in Figure 19. The term breakdown potential was chosen since, the test electrodes being embedded in epoxy resin, no distinction was made between pitting and crevice corrosion.

A linear relationship between the breakdown potential and the logarithm of the chloride ion concentration is observed for both materials. Several authors (*appendix 4*) have observed this kind of relationship. The lower breakdown potential values for the 12Cr-9Mn-C steel are not unexpected since the detrimental effect of manganese on the localised corrosion resistance of stainless steels is well known, and has led to its introduction with a negative coefficient in the pitting resistance equivalent (PRE) formulas (*appendix 4*). This negative effect of manganese is generally attributed to the presence of manganese sulphide inclusions.

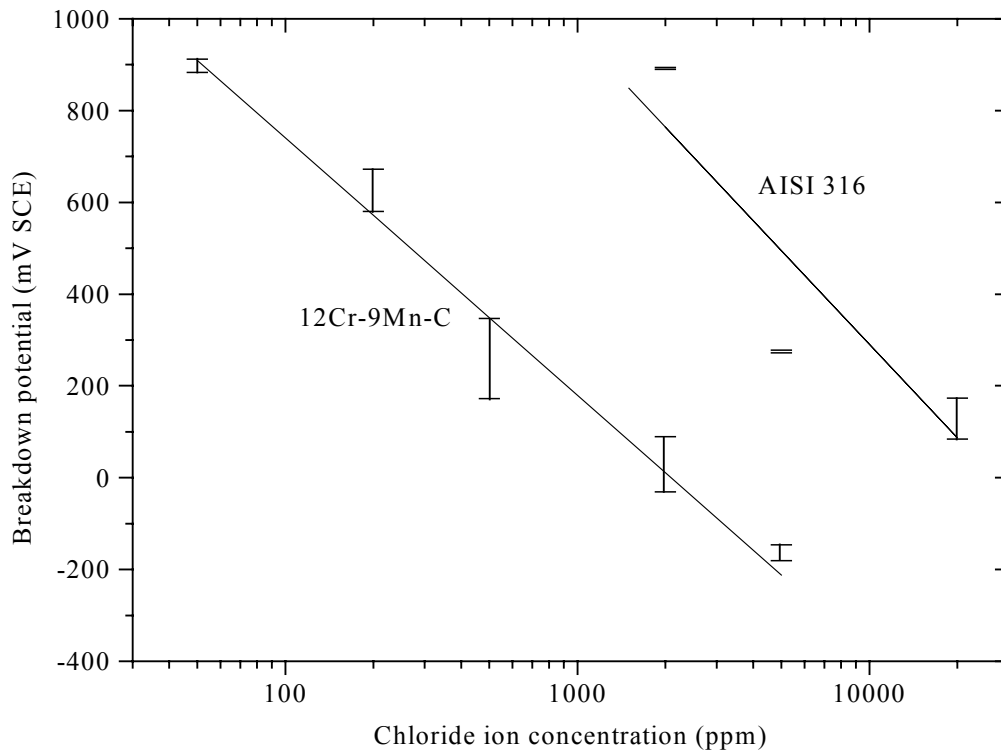


Figure 19. Breakdown potential as a function of chloride content

Although most of the mine waters have a chloride ion concentration below 500 ppm, the large hysteresis observed in the cyclic polarisation scans indicates that crevice corrosion will be a factor to take into consideration. Crevice corrosion is a common failure mode for stainless steel fasteners.

3.6 Bolt Calibration

Duplicate 750 mm long x 20mm diameter mini bolts were tensile tested and the load, strain, ferritescope, and longitudinal velocity values were recorded. A portable ultrasonic (USM 25 DAC) monitoring device was used to measure the longitudinal velocity during the calibration trials. The results show a good correlation between the longitudinal ultrasonic velocity and strain. The results are shown in Table 7. It can be seen that an increase in the amount of load (stress) results in an increase in longitudinal ultrasonic velocity.

When the stress on the bolts increases, the microstructure changes from non-magnetic to magnetic. The amount of magnetic phase increases when straining the alloy. As a comparison, the acoustic properties of several metals are listed in Table 8⁽¹¹⁾. The acoustic properties of metals and alloys are influenced by variations in structure and metallurgical condition. Therefore, for a given test piece, the properties may differ from the values listed in Table 8. The results in Table 7 are also illustrated in Figure 20. A good linear correlation between ultrasonic velocity and strain with an R^2 value of 0.96 was obtained.

Table 7. Ultrasonic velocity measurements of the stressed 20mm diameter mini bolts

Load (kN)	%Elongation	Ultrasonic velocity (m/s)	% Ferrite
0	0	5640	0
100	0.03	5643	0.24
110	0.05	5647	0.27
130	0.43	5652	0.34
150	0.81	5652	1.17
160	1.17	5657	1.29
180	2.45	5672	1.50
190	3.35	5676	2.02
200	5.2	5678	5.34
210	7.5	Fracture	14.49

Table 8. Acoustic properties of several metals⁽¹¹⁾

Stainless Steels	Density (ρ) g/cm ³	Sonic velocities (m/s)
Type 302	7.9	5660
Type 304L	7.9	5640
Type 347	7.91	5700
Type 410	7.67	5900
Type 430	7.7	6010

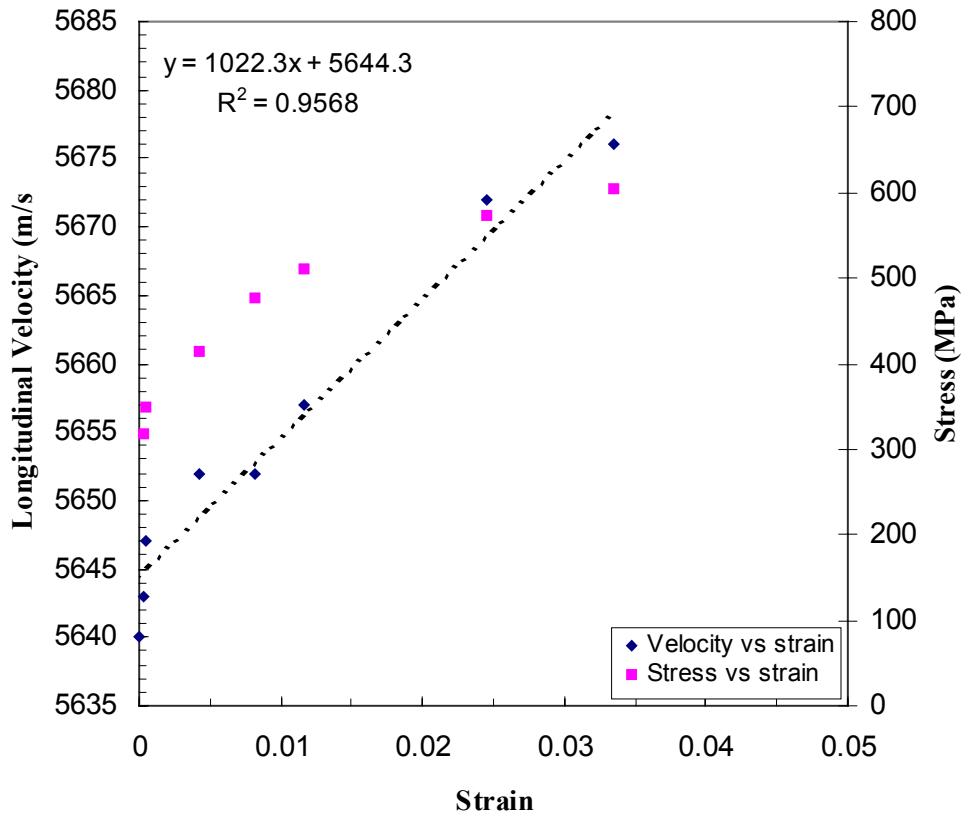


Figure 20. Longitudinal ultrasonic sound velocity versus strain of the smartbolt alloy

Performing bend tests on 450mm long by 20mm diameter mini bolts showed the effect of shear stresses. The mini bolts (see Figure 21a-b) were bent up to a load of 15kN and the velocity was measured. The results are shown in Table 9. Due to the fact that ultrasonic instrument measures using a time-of-flight and straight beam, the velocity decreases with bending angle. The results show that, using time-of-flight, a bent or even broken bolt can be detected in situ, provided that the original bolt length is known. Thus the technology can be used to detect overloaded, bent or broken bolts in-situ. If the sensitivity can be improved, it may even be used to check torque loads applied for tightening of bolts.

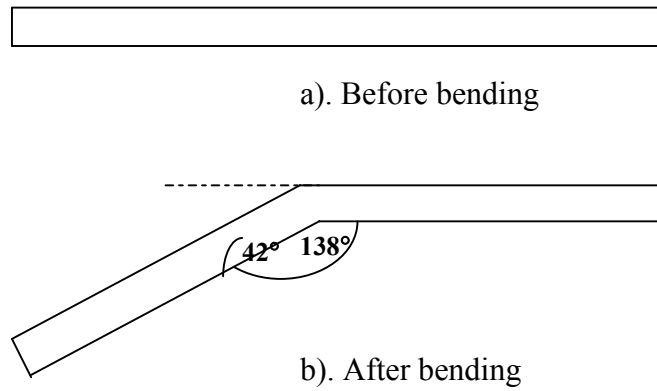


Figure 21. Schematics of 450mm mini bolt before and after bending

Table 9. Ultrasonic sound velocity measurement of the bent mini bolts

Load (kN)	Dimension (mm)	Bending Angle (°)	Ultrasonic velocity (m/s)
0	450mm x 20mm	180	5640
12	450mm x 20mm	158	4824
15	450mm x 20mm	138	4781

3.7 Field testing

The quality of the support system is of key importance to safety. The gully heading (location where the smartbolts are installed), are sometimes supported with rockbolts to counter rockfalls, whether induced by gravity or seismicity.

The chemically anchored bolt is the most common rock bolting system currently in use⁽¹²⁾. The modern system provides quick, easy and effective installation procedure. However, for this project, it is felt that the technology is more appropriate using anchoring rather than chemical or frictional forces. Also, it is important that the bolts do not slip once they have been installed.

The installation of a rock bolt is illustrated in Figure 22. It shows the drilling stage prior to installation of the required roofbolt. A hole is drilled to the appropriate diameter and depth and the bolt with expansion shell (anchor) is introduced into the hole; the bolt is pushed into the hole and tightened to an appropriate load.

The load is distributed to the surrounding rock by means of the base plate (Figure 23). The ultrasonic velocity of the bolt after installation is then measured using the ultrasonic instrument. The results are then superimposed on a calibration curve to obtain the amount of stress and strain the smartbolt and the surrounding rock experiences.



Figure 22. The drilling stage prior to installation of the required roofbolt at a platinum mine test site



Figure 23. Monitoring of a smartbolt (with a flat base plate) using an ultrasonic device

Loosening of rockbolt anchors after the blast appears to be a major problem in most of the mines. This is due to the current tensioning method, which is generally done manually with a simple tool such as a spanner. It was therefore agreed with the mine personnel to install the smartbolts using both chemical (cement) and expansion shells and to use a torque wrench for tensioning. However, during the installation a torque wrench was not used. The ultrasonic velocity results of the full size bolts, after three weeks and after three months of installation, are summarized in Table 10.

The smartbolt warning guideline modified by adding an extra column for ultrasonic velocity is shown in Table 11. Figure 24 show a bar chart of ultrasonic velocity of the bolts with warning guidelines superimposed on it. The results shown in Figure 24 show that the bolts except H and K are all in the elastic region. It can be seen from this figure that bolt H has developed a pattern in that it is gradually yielding. However, since mining has gradually moved away from that area of the stope, it is not expected to see much further change in the loading, with time.

Referencing to the calibration curve shown in Figure 20, the results indicates that the strain experienced by the bolts on installation was <0.01. After the first monitoring phase, bolt H showed a strain of above 0.01. No further monitoring was conducted on bolts A and F because that section of the mine was closed.

Table 10. Summary of the ultrasonic velocity results of smartbolts installed at platinum mine

Bolt ID	Length x diameter (mm)	Test site	Installation method	Ultrasonic velocity (m/s) After installation	Ultrasonic velocity (m/s) After three weeks	Ultrasonic velocity (m/s) After three months
A	1498 x 20	RPM	Cement	5648	#	#
B	1501 x 20	RPM	Cement	nd	#	#
E	1501 x 20	RPM	Cement	nd	#	#
F	1499 x 20	RPM	Cement	5648	#	#
H	1495 x 16	RPM	Anchor	5655	5663	5666
I	1498 x 16	RPM	Anchor	5648	5648	5648
K	1492 x 16	RPM	Anchor	5655	5655	5659
L	1500 x 16	RPM	Anchor	nd	nd	nd

nd → values were not taken due to improper installation, # → site was closed

Table 11. Potential Smartbolts warning guidelines

Reading (%Ferrite)	Comments	Ultrasonic sound velocity (m/s)
< 1	Stresses in elastic range	5640 to 5652
1 – 2	Bolt is yielding	5652 to 5672
2 – 5	Bolt is showing substantial plastic deformation	5672 to 5676
>5	Potentially dangerous situation	>5676

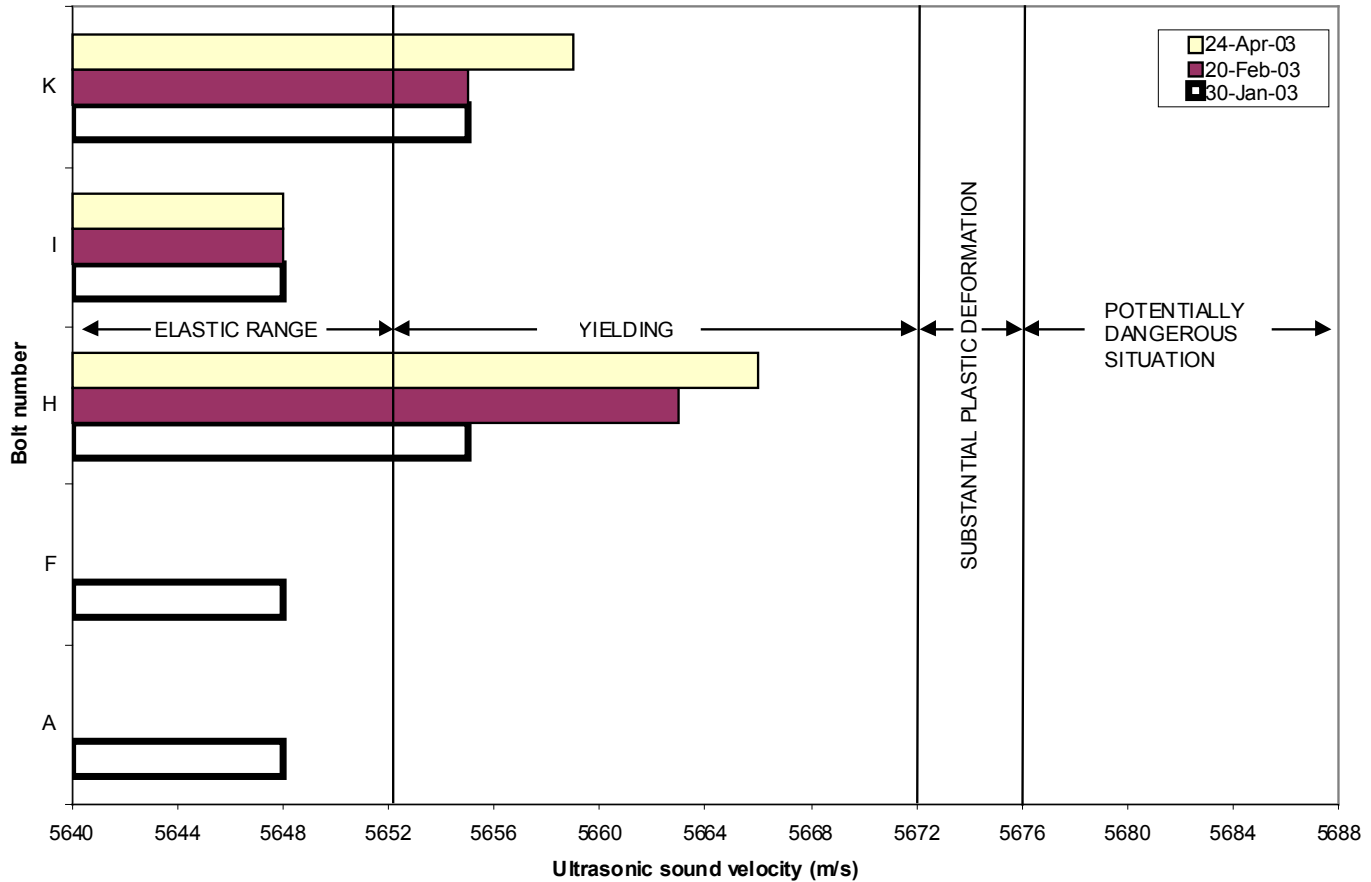


Figure 24. Graphical presentation of the results obtained from a platinum mine test site

4. CONCLUSIONS

- 4.1 An alloy composition has been identified as being suitable for acting as a smartbolt material under the influence of strain. Some problems do, however, exist with the ferritescope method of monitoring, in particular the depth of penetration.
- 4.2 The use of the smartbolt concept together with ultrasonic monitoring can be an effective and simple method of monitoring the load in a bolt. The readings are accurate and the technique should help to promote safety in the industry. Information can be gathered and logged quickly to determine whether bolts are bent, broken, or overloaded.

- 4.3 Ultrasonic methods appear to be a satisfactory method for interrogating smartbolts but the overall hardware package may need to be refined with continuing feedback from mining personnel.
- 4.4 Smartbolt alloy is particularly suited to application where corrosion is problematic

5. REFERENCES

- 1 Paton R., Moema J. and Fletcher CJ., 2000, Private Communication no. C3119M: *Development of a sensor material using Metastable Austenitic Stainless Steel.*, Mintek, Private Bag X3015, Randburg, 2125.
- 2 ASTM E8-99., *Test Method for Testing Testing of Metallic Materials*, American Society for Testing and Materials, West Conshohocken, USA, 2000
- 3 ASTM E494-75., *Standard Practice for Measuring Ultrasonic Velocity in materials*, American Society for Testing and Materials, West Conshohocken, USA, 2000
- 4 USM 25, Technical Reference and Operating Manual., Krautkramer., EN 12668-1
- 5 Metal Handbook, vol. 6, *Welding, Brazing and Soldering*, p.320, American Society for Metals, Ohio, USA, 1983.
- 6 Doege, E., Kulp, S., and Sunderkotter C., *Properties and Application of TRIP-steel in sheet metal forming*, Steel Research 73 (2002) no. 6 & 7., pp303-307
- 7 Apolostolos A., *et al.*, *Low-alloy TRIP steels: a correlation between mechanical properties and the retained autenite stability.*, Steel Research 73 (2002) no. 6 & 7., pp249-252
- 8 Fang, X.F., and W Dahl, Mater. Sci. Eng. A, 141, 189-198 (1991)
- 9 Smallman, R.E., *Mechanical properties*, Modern Physical Metallurgy , Third Edition, Butterworth & Co Publisher, LTD, London, 1970, 85
- 10 Ludwigson, D. C. and Berger, J. A., *Plastic behaviour of metastable austenitic stainless steels*, Journal of The Iron and Steel Institute, (1969) 413 – 419

- 11 ASM Handbook, vol. 17, *Ultrasonic Inspection*, Nondestructive Evaluation and Quality Control, ASM International, USA, 1989, p231
- 12 Daehnke, A., Acheampong, E., *et al.*, *Support Technologies to Cater for Rockbursts and Falls of Grounds in the Immediate Face Area*, SIMRAC Project GAP 606, CSIR: Division of Mining Technology. Auckland Park., South Africa.

APPENDIX 1

BACKGROUND INFORMATION ON THE USE OF ULTRASONIC TECHNIQUE

An area of growing interest is the use of ultrasound to monitor variations in microstructure⁽¹⁾. Ultrasonic velocity is a physical property influenced by microstructural features. A change in microstructure by the use of applied stress may be potentially monitored by accurately measuring longitudinal ultrasonic velocity, e.g., Kutty and co-workers⁽²⁾ showed that there is a variation of longitudinal ultrasonic velocity with ferrite content in a duplex stainless steel. A linear correlation was obtained (Figure 1).

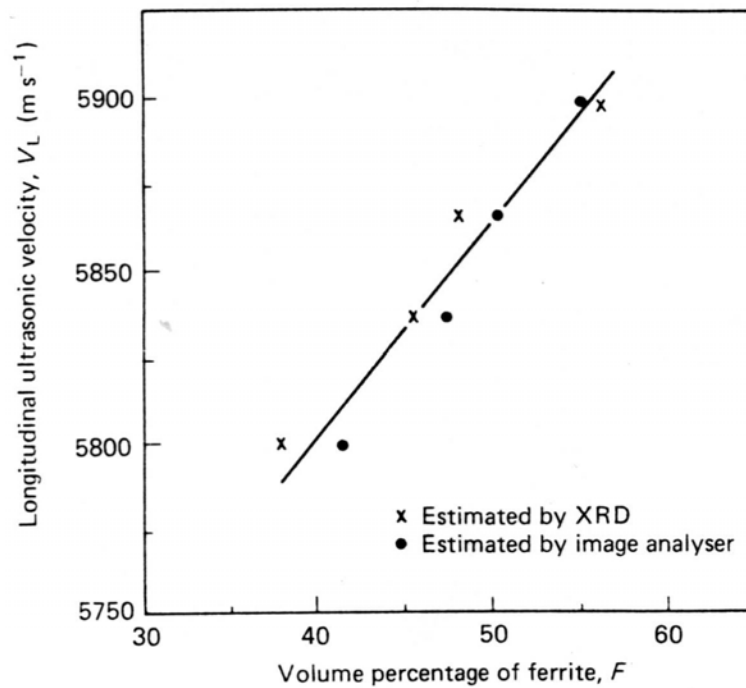


Figure 1: Variation of longitudinal ultrasonic velocity, V_L with ferrite content, F (vol %)

Certainly, ultrasonic longitudinal waves have excellent penetration and 1.5m long bolts should present no problem. Measurement is simple and fast. Test equipment is relatively cheap and easy to maintain and can be battery-operated to provide on-site inspection. Commercial instruments are available which also have data-logging facilities. When the level of magnetic phase being measured is low, it is inevitable that the precision and accuracy decrease. It may be that, in this case, ultrasonic techniques are preferable to magnetic methods.

The determination of sound velocity involves the measurement of sample thickness and the measurement of transit times with an A-scan display of ultrasonic echoes. The thickness of the samples and the velocity standard block are measured to an accuracy of ± 0.02 mm, and the A-scan display provides the relative time or distance between the interfacial and back echoes for the sample and the velocity standard. If the time sweep on the A-scan display is not accurately calibrated, the velocity standard provides the reference for comparing the relative transit times of the A-scan data. The bulk sound velocity of the sample can then be determined by comparing the A-scan spacing (transit times) of echoes in the sample to the echo spacing in the velocity standard.

All ultrasonic wall thickness measurements are based on a time-of-flight measurement. Accurate measurement results require a constant sound velocity in the test object. The variation in sound velocity is so slight that it is only of importance for high-precision measurements. If the test object is not homogeneous, the sound may propagate at different sound velocities in different part of the test piece. An average sound velocity should be taken in to account for the range calibration. This is achieved by means of a reference block whose sound velocity corresponds to the average sound velocity of the test block.

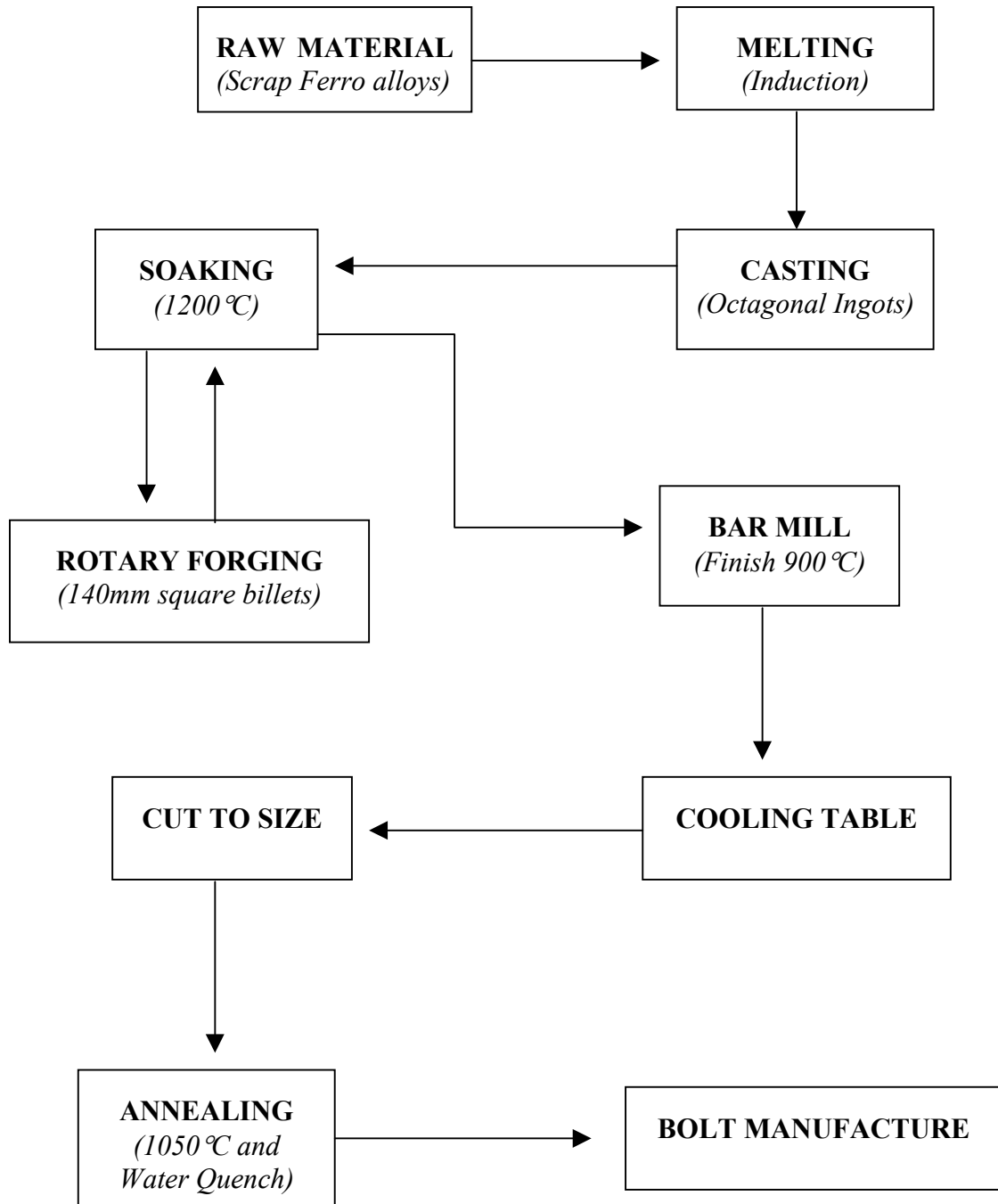
If substantial sound velocity variations are to be expected, then the instrument calibration should be readjusted to the actual sound velocity values at shorter time intervals.

REFERENCES

- 1 Sharpe, RS, Non-destructive Ultrasonic Testing, Chartered Mechanical Engineer June 1979, pp. 65-68.
- 2 Kulty, TRG, *et al*, *Use of Ultrasonic Velocity for Nondestructive Evaluation of Ferrite Content in Duplex Stainless Steels*, NDT International, Vol. 20, Number 6, Dec. 1987, pp. 359-361.

APPENDIX 2

PRODUCTION ROUTE OF SMARBOLT ALLOY



APPENDIX 3

OPERATION OF THE KRAUTKRAMER USM 25 ULTRASONIC SOUND VELOCITY-MEASURING INSTRUMENT.

1. Purpose

The purpose of this document is to describe the basic set-up and operation of Krautkramer USM 25 ultrasonic sound velocity measuring instrument.

2. Scope

This procedure covers the initial set-up, operation and calibration of the equipment only.

3. Procedure

3.1 Descriptions of the connections

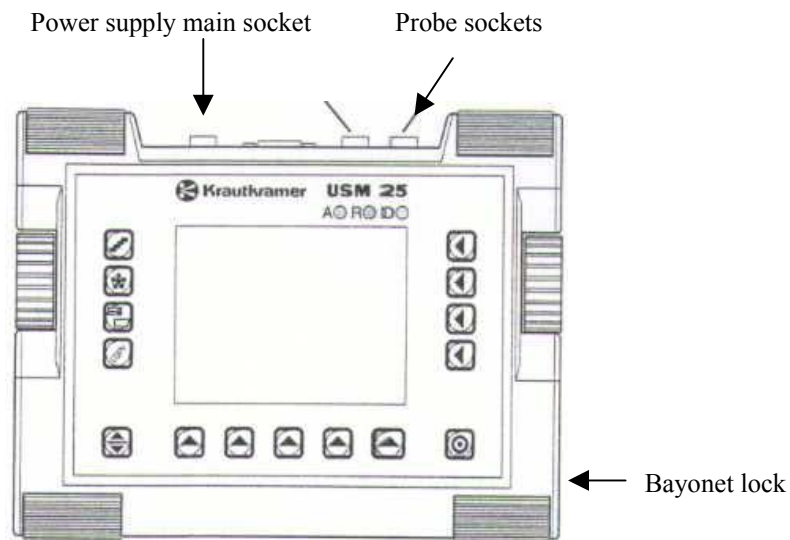


Figure 1. Connecting terminals for USM 25 instrument

3.1.1 Power supply unit

The USM 25 can be powered either via a main supply using a transformer or with rechargeable batteries. The batteries need not be removed if main power is utilized, as the battery power is automatically isolated. The transformer is connected to the USM 25 at the top left of the unit.

3.1.2 Operation using batteries

The battery compartment is located at the bottom of the instrument; the opening with the Bayonet lock cap is on the right. The measurement line of the USM 25 indicates an inverted B if the battery voltage is too low.

3.1.3 Connecting a probe

To prepare the USM 25 for operation, a probe has to be connected to the sockets at the top right on the instrument casing. Both connector sockets are equally suitable (connected in parallel) for connecting probes equipped with only one ultrasonic element (ultrasonic transducer) therefore it does not matter which one of the two sockets is used.

3.2 Descriptions of the front panel keys

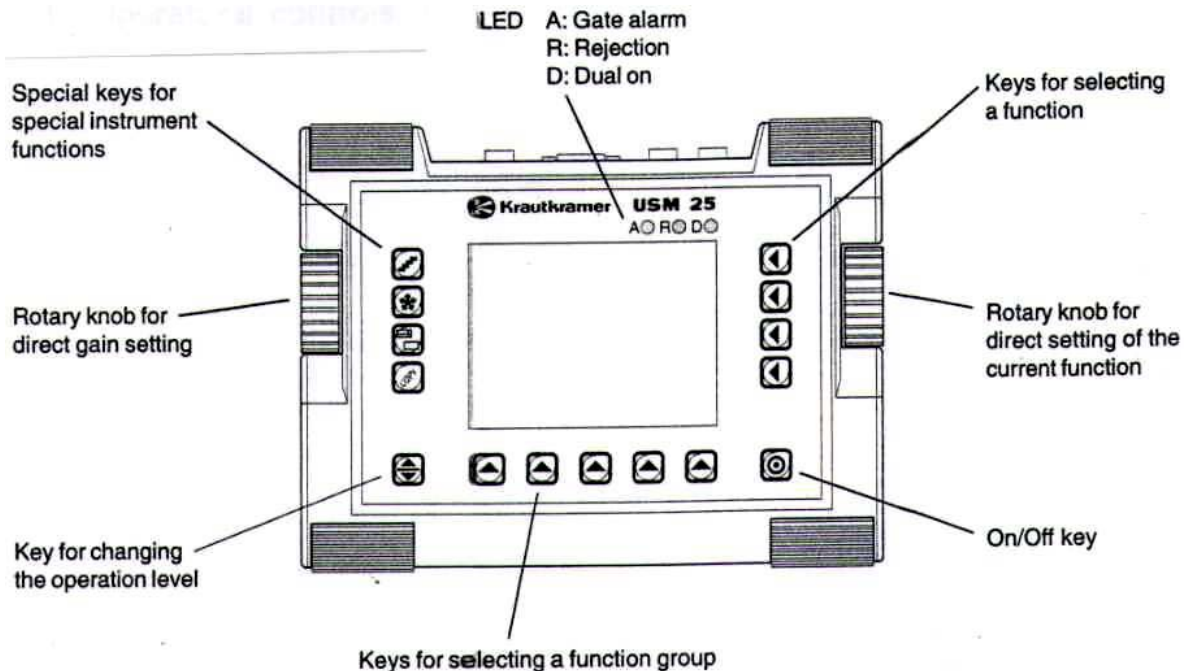


Figure 2. Operator's controls

3.2.1 Starting the USM 25

To start the USM 25, press the switch-on key (see *Figure 2*)

The instrument will carry out a self-check and then switches over to stand-by mode.

The function values and basic settings (language and units) are set as defaults by the factory.

3.2.2 Operational concept

The use of USM 25 is a user friendly instrument. It has three operating levels, which can be accessed by pressing the $\uparrow\downarrow$ key. The active operating level will be recognised by the number on the separation line between the first and the second group.

Each operating level contains five function groups.

First operating level

BASE 1	PULS	RECV	aGAT	bGAT
---------------	-------------	-------------	-------------	-------------

Second operating level

CAL 2	DAC	TRIG	MEM	DATA
--------------	------------	-------------	------------	-------------

Third operating level

MEAS 3	MSEL	LCD	CFG 1	CFG 2
---------------	-------------	------------	--------------	--------------

3.2.3 Overview of the functions

BASE: The functions found here are required for the basic adjustment of the screen display.

PULS: Combined in this group are the functions that serve for the adjustment of pulser.

RECV: Combined in this group are the functions that serve for the adjustment of receiver.

aGAT: All functions for setting the gate A can be found in this group

bGAT: All functions for setting the gate B can be found in this group


- CAL:** This function group makes functions for the semiautomatic calibration available.
- DAC:** This is a function group where the functions for the DAC can be set.
- TRIG:** Combined in this group are the functions required for angle beaming using angle-beam probes for the display of a (reduced) projection distance and depth position of a reflector (for plane-parallel and circular curved components).
- MEM:** These functions serve for sorting, loading and deleting of data sets
- DATA:** The functions of this group serve for the data-set management and documentation
-
- MEAS:** In this group, it is possible to define the measuring point, select a parameter for the zoomed measured-value display in the A-scan as well as for the setting of the Magnify function, and select different settings for the A-scan.
- MSEL:** This is where the measurement line is confirmed. One display for each of the four positions can be chosen.
- LCD:** This is the function group where the LCD contrast can be set and backlight as well as the echo display mode on the screen.
- CFG1:** Functions for the configuration: unit dialog language, printer driver and assignment of the **copy** key.
- CFG2:** Other functions for the configuration: time and date, alarm horn; moreover, changing from the DAC over to the DSG evaluation mode (only USM 25S).

3.3 Adjusting the display range (function group **BASE**)

The function group **BASE** enables the basic adjustment of the display range. The display on the screen must be adjusted for the material to be tested (function **MTLVEL**) and for the probe used (function **P-Delay**). In addition the range for the measurement and display start point must be chosen.

3.3.1 RANGE (Display range)


The range for your measurement can be adjusted in **RANGE**. This adjustment depends on the frequency range setting (function **FREQU**).

- Use  button to select the function **RANGE** and adjust the required value by means of the right-hand rotary knob.

The range limits are also dependent on the set sound velocities (function **MTVEL**): with small values for c , the range limits are shifted downwards, with large values upwards.

3.3.2 MTLVEL (Material velocity)

In **MTVEL**, the sound velocity in the test object can be selected. This can be one of two predefined fixed values, or a continuously variable value.

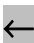
- Use  button to select the function **MTVEL** and adjust the required value by means of the right-hand rotary knob.

Always ensure that the function **MTVEL** is correctly set. The USM 25 calculates all range and distance indications on the basis of the value adjusted here.

3.3.3 D-DELAY (Display starting point)


In **D-DELAY** the choice of whether to display the adjusted range (for example 250mm) starting from the surface of the test object, or in a section of the test object starting at a later point can be made. This allows you to shift the complete screen display and consequently also the display zero point.

If the display should for example start from the surface of the test object, the value in **D-DELAY** must be set to 0.

- Use  button to select the function **D-DELAY** and adjust the value for the display starting point by means of the right-hand rotary knob

3.3.4 P-DELAY (Probe delay)


Every probe has a delay line between the transducer element and the coupling face. This means that the initial pulse must first pass through this delay line before the sound wave can enter the test object. Compensation can be made for this influence of the delay line in the function **P-DELAY**.

- Use  button to select the function **P-DELAY** and adjust the value for the probe delay by means of the right-hand rotary knob


3.4 Setting the gates (function groups aGAT and bGAT)

All functions for setting the (dual) gate are arranged in the function group **aGAT** and **bGAT**. The task of the gates is to monitor the range of the test object where you expect to detect a flaw. If an echo exceeds or falls below the gate, an alarm signal is output via the LED A. The gate chooses the echo for the digital time-of-flight or amplitude measurement. The measured value is indicated in the measurement line.

The starting point of the gates A or B can be fixed within the adjustment range of 0 to max. 9999 mm /250”.

- Use  button to select the function **aSTART** or **bSTART** and then use the right-hand rotary knob to adjust the required settings.

The gate width can be determined within the range of 0.2 to 9999 mm / 0.008 to 250”.

- Use  button to select the function **aWIDTH** or **bWIDTH**, and then use the right-hand rotary knob to adjust the required value.

3.5 Calibrating the USM 25

Before working with the USM 25, calibration of the instrument must be carried out. The material velocity and display range must be adjusted and allowance made for the probe delay depending on the material and dimensions of the test object.

To ensure a safe and proper operation of the USM 25, it is necessary that the operator be adequately trained in the field of ultrasonic testing technology.

In addition, the USM 25 has a semiautomatic calibration function, which is described in Case B below.

The sound path measurement in either the calibration process or in the subsequent echo evaluation process depends on the choice of the measuring point which can be set either to flank or to peak in the USM 25. In principle, the peak measurement should be preferred because the measured distances do not depend on the echo height in that case.

3.5.1 Case A: Calibrating with known material velocity

Calibration process:

- Set the known material velocity in **MTLVEL** (function group **BASE**)
- Couple the probe to the calibration block (use Teepol soap as couplant).
- Set the required display range in **RANGE** (function group **BASE**). The calibration echo must be displayed on the screen.
- Position the gate on one of the calibration echoes until the sound path of the echo is indicated in the measurement line.
- After this, change the adjustment of the function **P-DELAY** (function group **BASE**) until the correct sound path for the selected calibration echo is indicated in the measurement line.

Example:

Calibration is being carried out for the calibration range of 100mm via the function group **BASE** using the calibration block V1 (thickness 25mm) which is laid flat-wise.

- Set the **RANGE** to 100mm
- Set the known material velocity of 5920m/s in **MTLVEL**.
- Set the gate so that it is positioned on the first calibration echo (from 25mm).
- Read the sound path in the measurement line. If this value is not equal to 25mm, change the adjustment for the function **P-DELAY** until it is at 25mm.

This completes the calibration of the USM 25 to the material velocity of 5920m/s with a calibration range of 100mm for the probe used.

3.5.2 Case B: Calibrating with unknown material velocity

Use the semiautomatic calibration function of the USM 25 via the function group **CAL** for this calibration case.

The distance between 2 calibration echoes must be entered as default data. The USM 25 will then carry out a plausibility check, calculate the material velocity and the probe delay, and set the parameters.

Calibration process:

- Set the required display range in **RANGE** (function group **BASE**). The two calibration echoes selected must be displayed on the screen. Set the range so that the second calibration echo is located on the right edge of the screen.
- Select the function group **CAL** using **↑**.
- Enter the distances of the two calibration echoes in **S-REF1** and **S-REF2**.
- Position the gate (function **aSTART**) on the first calibration echo.
- Press **copy** to record the first calibration echo.
- The recording of the calibration echo is confirmed by the message “**Echo is recorded**”, and the function **CAL** indicates the value 1.
- Move the gate to the second calibration echo
- Press **copy** to record the second calibration echo.

The correct calibration is confirmed by the message “**Calibration is done**”. The material velocity and probe delay are calculated and set. The value of the **CAL** function goes back to 0.

Example:

- Enter the distance (thickness) of the two calibration lines **S-REF1** (20mm) and **S-REF2** (40mm)
- Position the gate on the first calibration gate.
- Press **copy** to record the first calibration echo.
- Position the gate on the second calibration gate.
- Press **copy**

The second echo is stored, the calibration is carried out, and the **CAL** function is reset to 0.

The valid calibration is briefly confirmed and carried out.

If you select the function group **BASE**, the material velocity and probe delay can be read.

APPENDIX 4

CORROSION PROPERTIES OF SMARTBOLT ALLOY

1. Experimental

The corrosion performance of the 12Cr-9Mn-C alloy (smartbolt) was evaluated in synthetic mine water and compared with that of AISI 304 and 316 as well as mild steel.

Mintek^(1,2) surveyed the corrosivity of waters in South African gold mines and developed three typical artificial mine waters, labelled 'A', 'B' and 'C'. The mine water used in this investigation was mine water 'B'. It is an artificial machine water typical of that usually found flowing through the general reticulation system of a mine. This artificial water is based on samples of machine water taken from the Free State gold field, where corrosion problems tend to be greater than those experienced on the Witwatersrand. The composition of this synthetic mine water is given in Table I.

Table 1. Composition of the synthetic mine water (pH = 6.5)

	mg/l
NaHCO ₃	42
CaSO ₄ .2H ₂ O	1290
MgSO ₄ .7H ₂ O	608
NaCl	2040
Na ₂ SO ₄	142
NH ₄ NO ₃	317
KNO ₃	216
KNO ₂	60
FeSO ₄ .7H ₂ O	15
Kaolin	45

The corrosion rates were measured at different pH values, while the localised corrosion performance was evaluated at the normal value of pH 6.5 with different chloride contents. The pH was changed by adding sulphuric acid or sodium hydroxide, and the chloride content was altered by adding sodium chloride.

A PC-driven 'ACM AutoTafel' potentiostat was used to perform the electrochemical tests. The test electrodes were discs, 2 cm in diameter, ground to a 120-grit finish and embedded in epoxy resin. Two graphite rods were used as counter electrodes and a Haber-Luggin capillary made the junction with a saturated calomel reference electrode (SCE). All the potential values were measured with respect to the SCE.

To determine the corrosion rates, a Tafel plot was recorded from -0.2 V to 0.2 V versus the corrosion potential at a scanning speed of 0.01 V/min. The corrosion current was determined by Tafel extrapolation of the rate-determining segment, and the corrosion rate calculated by introducing the correct values of density and equivalent weight.

When the corrosion rate was measured as a function of time, the Linear Polarisation Resistance (LPR) technique was used so that the test electrode was only slightly disturbed from its equilibrium conditions. In this case, the potential was varied from -0.01 V to 0.01 V versus the corrosion potential at a scanning speed of 0.01 V/min. A value of 0.02 V⁽³⁾ was used for the B constant in the Stern and Geary formula. A LPR measurement was recorded every 6 hours for approximately 40 hours.

The LPR technique was also used to measure the corrosion rate of the 12Cr-9Mn-C alloy at pH 3, since at that pH value it showed an active to passive transition and Tafel extrapolation was not possible.

Cyclic polarisation scans were also conducted to evaluate the localised corrosion resistance. The scanning speed was 0.01 V/min and the scan direction was reversed at a current density of 5×10^{-4} A/cm². All tests were conducted at 30 °C under stirring conditions.

2. Results and discussion

The corrosion rates of the various materials are given as a function of pH in Table II and represented graphically in Figure 1.

The corrosion rate of the 12Cr-9Mn-C steel (smartbolt alloy) is more than two orders of magnitude lower than that of mild steel and one order of magnitude higher than that of AISI 316. The value close to 0.01 mm/y over a large pH range is quite acceptable, but the corrosion rate increases sharply below pH 4. However, measurements of the corrosion rate of the 12Cr-9Mn-C steel and AISI 316 as a function of time at pH 3 (Figure 2) indicate that in the case of the 12Cr-9Mn-C steel, the corrosion rate drops significantly in the first 10 hours and reaches the value observed at higher pHs. The potential increases from -0.050 V to -0.025 V, and it appears thus that some passivation is taking place.

Figure 3 compares the corrosion rates as a function of the raw materials cost (October 1998). It can be seen from Figure 3 that an initial threefold increase in cost (12Cr-9Mn-C compared to mild steel) lowers the corrosion rate by more than two orders of magnitude, but that a further threefold increase in cost only reduces the corrosion rate by a factor of three. This places the 12Cr-9Mn-C steel in a very favourable position.

Table II. Corrosion rate values

Material	Corrosion Rate (mm/y)			
	pH 3	pH 5	pH 7	pH 9
Mild Steel	17.4	1.7	1.6	2.9
12Cr-9Mn-C (smartbolt alloy)	2.5	0.020	0.0070	0.0072
AISI 304	0.0023	0.0019	0.0033	0.0014
AISI 316	0.0013	0.0011	0.0016	0.0006

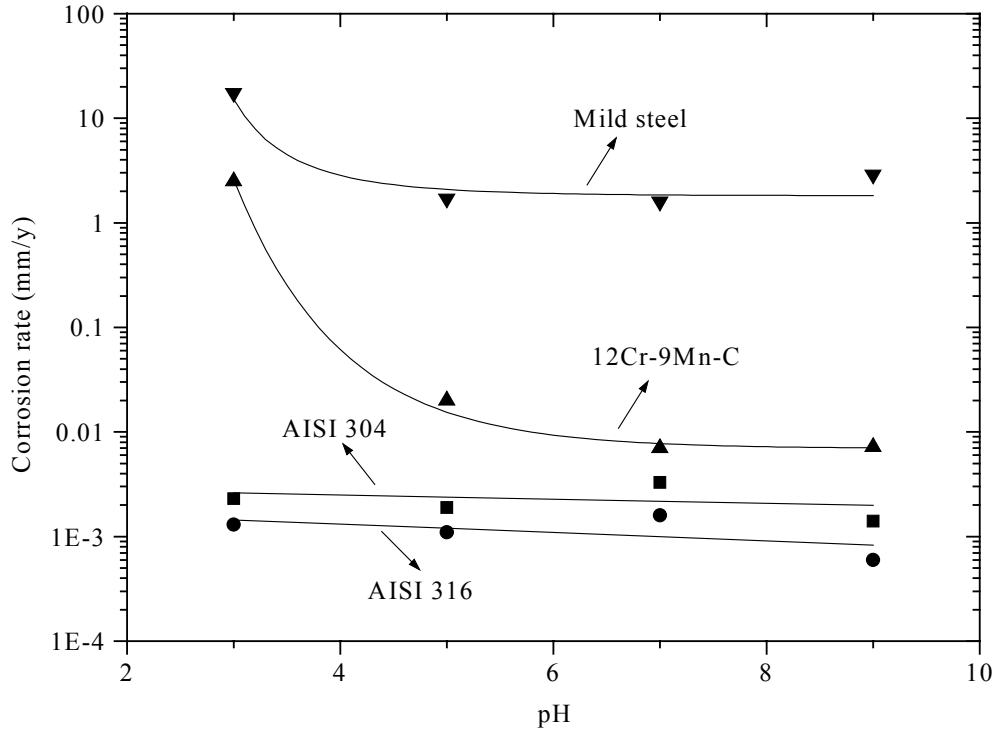


Figure 1. Corrosion rates as a function of pH

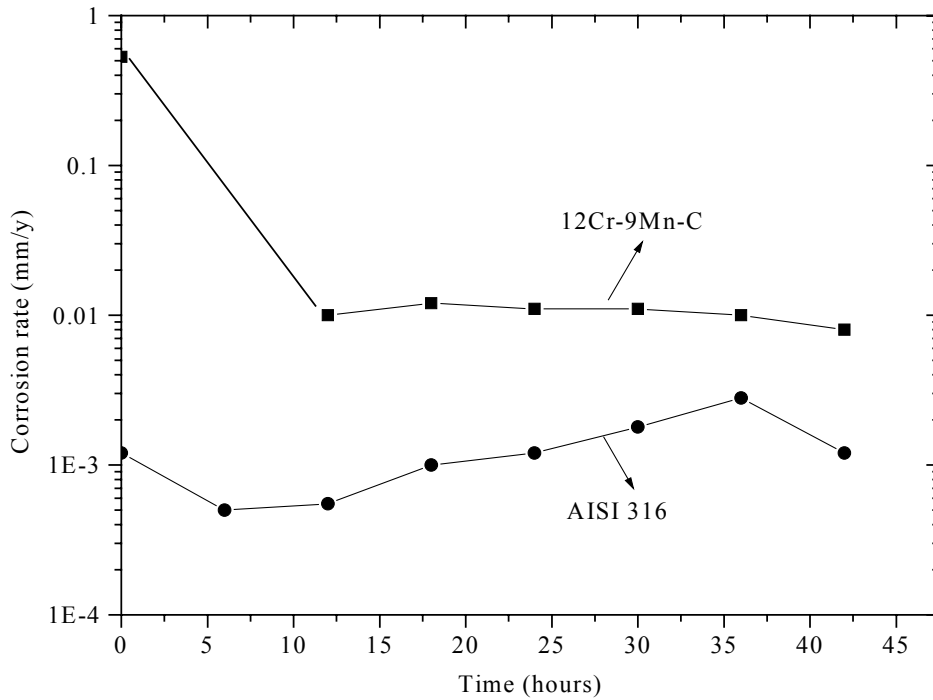


Figure 2. Corrosion rates as a function of time (pH 3)

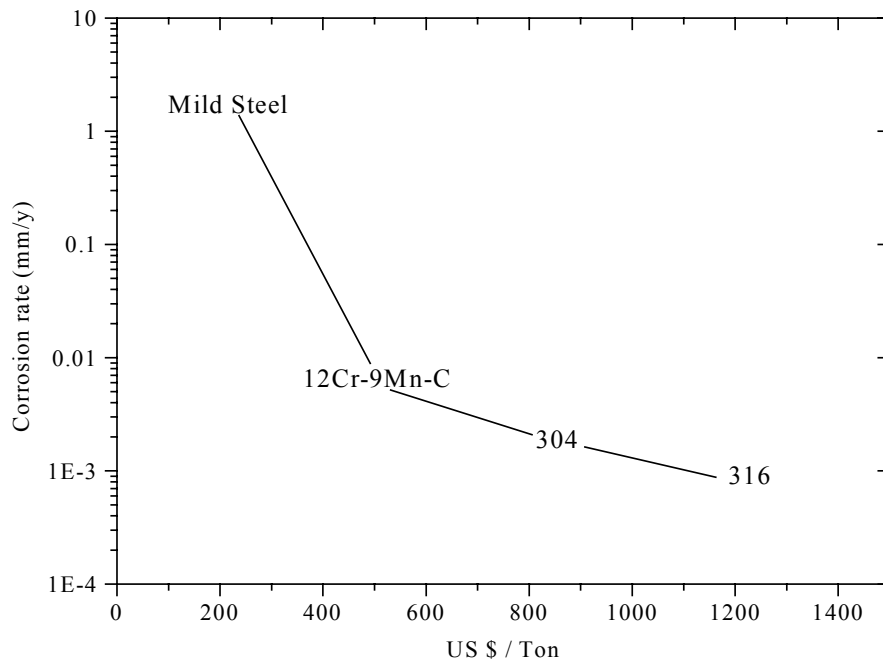


Figure 3. Corrosion rates as a function of the raw materials cost

The breakdown potential values of the 12Cr-9Mn-C steel and AISI 316, determined from cyclic polarisation scans in mine water with various chloride concentrations, are given in Table III and represented graphically in Figure 4. The term breakdown potential was chosen since, the test electrodes being embedded in epoxy resin, no distinction was made between pitting and crevice corrosion.

Table III. Breakdown potential values

Cl ⁻ concentration (ppm)	E _{Break} (mV SCE)	
	12Cr-9Mn-C (smartbolt alloy)	AISI 316
50	912	-
	883	
200	580	-
	672	
500	347	-
	172	
2000	-31	894
	89	890
5000	-181	278
	-146	272
20000	-	173
		84

A linear relationship between the breakdown potential and the logarithm of the chloride ion concentration is observed for both materials. Several authors^(4,5) have observed this kind of relationship. The lower breakdown potential values for the 12Cr-9Mn-C steel are not unexpected since the detrimental effect of manganese on the localised corrosion resistance of stainless steels is well known, and has led to its introduction with a negative coefficient in the pitting resistance equivalent (PRE) formulas^(6,7). This negative effect of manganese is generally attributed to the presence of manganese sulphide inclusions and several authors⁽⁸⁻¹⁰⁾ have described in details the mechanism of attack.

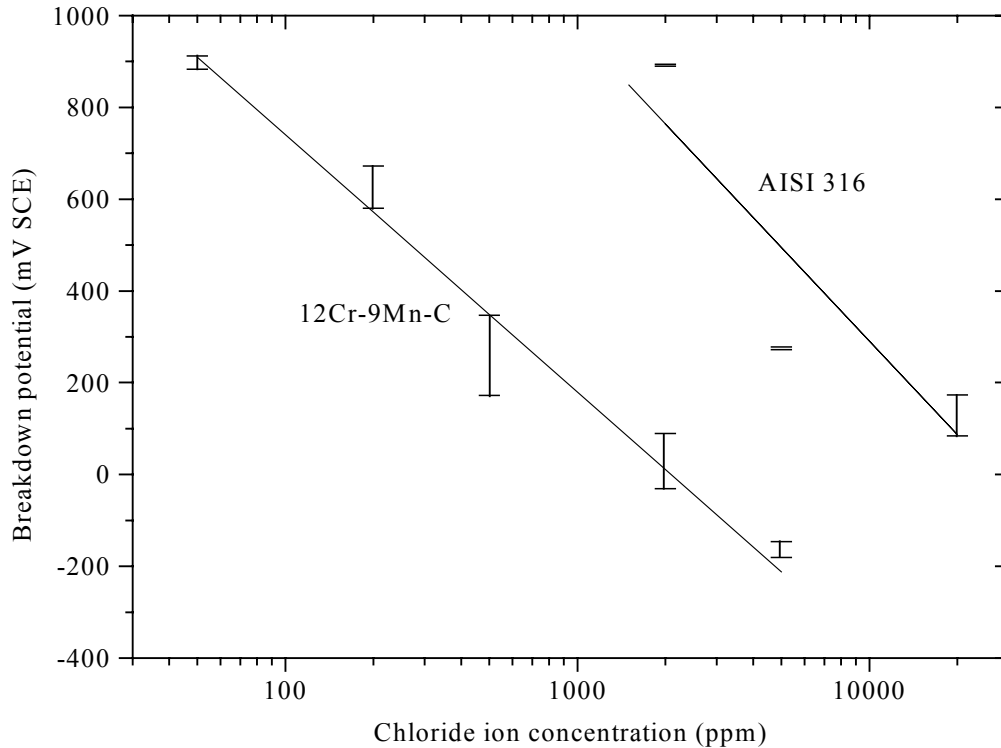


Figure 4. Breakdown potential as a function of chloride content

Although most of the mine waters have a chloride ion concentration below 500 ppm, the large hysteresis observed in the cyclic polarisation scans indicates that crevice corrosion will be a factor to take into consideration. Crevice corrosion is a common failure mode for stainless steel fasteners.

3. References

- (1) A. Higginson and R.T. White, "A preliminary survey of the corrosivity of waters in gold mines", Mintek report N° M65, Randburg, South Africa, (1983)
- (2) A. Higginson, "The effect of physical and chemical factors on the corrosivity of a synthetic mine water", Mintek report N° M140, Randburg, South Africa, (1984)
- (3) R. Grauer, P.J. Moreland and G. Pini, "A literature review of polarisation resistance constant (B) values for the measurement of corrosion rates", NACE, Houston, (1982)
- (4) H.P. Leckie and H.H. Uhlig, *J. Electrochem. Soc.*, **113**, p.1262, (1966)
- (5) Z. Szklarska-Smialowska, "Pitting corrosion of metals", NACE, Houston, (1986)

- (6) G. Ronelli, B. Viantini, and A. Cigada, *Materials and Corrosion*, **46**, p.628, (1995)
- (7) R.F.A. Jargelius-Petterson, *Corrosion*, **54**, P.162, (1998)
- (8) G.S. Eklund, *J. Electrochem. Soc.*, **121**, p.467, (1974)
- (9) K.J. Blom and J. Degerbeck, *Materials Performance*, **22** (7), p.52, (1983)
- (10) Z. Scklarska-Smialowska and E. Lunarska, *Werkst. Korros.*, **32**, p.478, (1981)

DISTRIBUTION

Dr PP Jourdan

Dr NA. Barcza

Dr RL. Paul

Dr M Motuku

Mr JJ McEwan

Dr LA Cornish

Mr R Paton

Mr JC Kerr

Mr S Roberts

Mr CJ Fletcher

Mr JS Moema

Mr D Adams (3 copies)

SAFETY IN MINES RESEARCH ADVISORY COMMITTEE

Private Bag X63

Braamfontein

2107

RSA

Library

File: 73089901